Acta Materialia 118 (2016) 28–43

Contents lists available at ScienceDirect

Acta Materialia

journal homepage: www.elsevier.com/locate/actamat

Full length article

Study of lattice strain evolution during biaxial deformation of stainless steel using a finite element and fast Fourier transform based multi-scale approach

M.V. Upadhyay [a], S. Van Petegem [a], T. Panzner [b], R.A. Lebensohn [c], H. Van Swygenhoven [a, d, *]

[a] Swiss Light Source, Paul Scherrer Institute, CH-5232 Villigen PSI, Switzerland
[b] Laboratory for Neutron Scattering, NUM, Paul Scherrer Institute, CH-5232 Villigen PSI, Switzerland
[c] Materials Science and Technology Division, Los Alamos National Laboratory, Los Alamos, NM 87545, USA
[d] Neutrons and X-rays for Mechanics of Materials, IMX, Ecole Polytechnique Federale de Lausanne, CH-1012 Lausanne, Switzerland

ARTICLE INFO

Article history:
Received 12 April 2016
Received in revised form
15 June 2016
Accepted 15 July 2016

Keywords:
Biaxial stresses
Lattice strains
Multi-scale modeling
Finite element
Neutron diffraction

ABSTRACT

A multi-scale elastic-plastic finite element and fast Fourier transform based approach is proposed to study lattice strain evolution during uniaxial and biaxial loading of stainless steel cruciform shaped samples. At the macroscale, finite element simulations capture the complex coupling between applied forces in the arms and gauge stresses induced by the cruciform geometry. The predicted gauge stresses are used as macroscopic boundary conditions to drive a mesoscale elasto-viscoplastic fast Fourier transform model, from which lattice strains are calculated for particular grain families. The calculated lattice strain evolution matches well with experimental values from in-situ neutron diffraction measurements and demonstrates that the spread in lattice strain evolution between different grain families decreases with increasing biaxial stress ratio. During equibiaxial loading, the model reveals that the lattice strain evolution in all grain families, and not just the 311 grain family, is representative of the polycrystalline response. A detailed quantitative analysis of the 200 and 220 grain family reveals that the contribution of elastic and plastic anisotropy to the lattice strain evolution significantly depends on the applied stress ratio.

1. Introduction

Metals and alloys used for engineering applications often experience biaxial stress states during their fabrication or under service conditions. Their macroscopic yield and subsequent plastic behavior significantly depends on this applied biaxial stress state. However, most of our knowledge on material behavior is derived from uniaxial deformation tests. Relying solely on uniaxial tests may result in an erroneous description of biaxial mechanical behavior for these materials.

The past few decades have seen an increasing trend towards the development and use of biaxial mechanical testing techniques (see Ref. [1] and references within). Biaxial testing on cruciform shaped samples has proven to be particularly useful in characterizing the macroscopic behavior of materials [2–7]. The cruciform shape has the advantage of applying any arbitrary stress ratio in both tension and compression. This allows access to a large portion of the 2-dimensional stress space without changing the experimental setup. However, Makinde and co-workers [8–10] noted that an analytical computation of the gauge stresses in a cruciform sample is not simply the force divided by area. Hoferlin et al. [11] used finite element (FE) simulations to show that the cruciform geometry results in a coupling between the forces in the arms and the gauge stresses. For instance, FE simulations of Bonnand et al. [12] and Claudio et al. [13] showed that for a cruciform geometry similar to the one used in this study a uniaxial load in the arm results in biaxial gauge stresses with a compressive component normal to the loading direction. Based on this, FE modeling has been used to study the evolution of gauge stresses in different cruciform geometries [14,15] and optimize the cruciform geometry shape [16]. Foecke and co-workers proposed to use an x-ray diffractometer to measure multiaxial stresses and corresponding yield loci [17–19].

* Corresponding author.
E-mail address: helena.vs@psi.ch (H. Van Swygenhoven).

http://dx.doi.org/10.1016/j.actamat.2016.07.028

At the microstructural level, elastic and plastic anisotropy of polycrystalline aggregates result in a heterogeneous distribution of internal stresses and strains. In recent years, in-situ synchrotron x-ray and neutron diffraction have become well established techniques to measure the lattice strain evolution for differently oriented grain families [20]. This is achieved by tracking changes in lattice spacing through diffraction peak position shifts. Collins et al. [21] used in-situ synchrotron x-ray diffraction to study lattice strain and texture evolution during biaxial tensile deformation of cruciform samples made from cold rolled low carbon ferritic steel. They showed that the lattice strain evolution as a function of the azimuthal angle is highly dependent on the applied biaxial stress ratio. The role of cruciform geometry on the macroscopic stress state was however not addressed. Recently, a unique biaxial testing rig was designed and installed in the POLDI neutron beamline at the Paul Scherrer Institute in Switzerland [22]. Using this machine, a series of in-situ neutron diffraction measurements were performed on 316L stainless steel cruciform samples (also used in this work) subjected to biaxial monotonic loading and strain path changes [22,23]. It was found that lattice strain evolution under monotonic equibiaxial tension is significantly different from uniaxial tension. Furthermore, the lattice strain evolution differs when deforming uniaxially a cruciform sample or a dog-bone sample. However, a quantitative analysis of the applied stress ratio on the lattice strain evolution was not performed.

A quantitative understanding of the relation between the applied stress ratio and the lattice strain can be achieved by combining in-situ diffraction studies with crystal plasticity modeling. In this regard, a number of advanced polycrystal plasticity models are available: the small strain elasto-plastic self consistent [24], the finite strain elasto-plastic self consistent [25,26], the elasto-viscoplastic self consistent [27], the elasto-viscoplastic fast Fourier transform (EVPFFT) [28,29] and the crystal plasticity FE [30] models. In this work, the EVPFFT model of Lebensohn and co-workers [28,29] is used. In contrast to mean field self-consistent approaches, EVPFFT is a full field approach that accounts for elastic and plastic grain neighborhood interactions. Furthermore, it is computationally faster than the crystal plasticity FE model. However, EVPFFT is designed to study representative cubic volume elements of polycrystals subjected to strain rate or stress boundary conditions; capturing directly the macroscopic biaxial stress evolution in the cruciform gauge region under the action of experimental forces or displacements is therefore beyond the scope of this model.

To circumvent this limitation, we propose using the following multi-scale approach. The experimental biaxial load and displacement boundary conditions on cruciform samples are supplied to the commercial finite element simulation software ABAQUS [31]. The predicted surface strains are compared with those obtained from digital image correlation (DIC) measurements. The predicted macroscopic field variables are averaged over the neutron irradiated gauge volume and supplied as macroscopic boundary conditions to the meso-scale EVPFFT model. Lattice strains calculated using the EVPFFT model are then compared with those obtained from in-situ neutron diffraction measurements. The proposed synergetic combination of multi-scale FE and EVPFFT, henceforth known as FE-FFT, modeling and experiments is shown in Fig. 1. To the author's knowledge such an FE-FFT approach has not yet been used to study lattice strain evolution during uniaxial or biaxial loading using experimental boundary conditions. Note that recently Kochmann et al. [32] proposed an integrated FE-FFT and phase field approach to study austenite to martensite transformation.

The main objective of this work is to use the FE-FFT approach to obtain a quantitative understanding of the load dependence of lattice strain evolution during uniaxial and equibiaxial monotonic loading tests performed on 316L stainless steel cruciform samples [22]. The paper is divided into sections as follows. In Section 2 the relevant properties of 316L stainless steel are recalled along with the in-situ neutron diffraction technique to measure lattice strains. Then the cruciform sample geometry studied in this work is presented along with the details of the monotonic loading tests performed. Section 3 presents the multi-scale FE-FFT model and the passage of information between experiments and simulations. The simulation procedure and material parameters used at both length scales are described. Section 4 compares the FE-FFT model with the experimental observations. In Section 5, a detailed analysis of the lattice strain evolution of 200 and 220 grain families is performed to obtain a quantitative understanding of their load dependence. Section 6 presents the main conclusions from this study. A biaxial stress ratio dependent expression for the directional elastic compliance is proposed in the appendix. Throughout this document, upper case letters will be used to denote macroscopic mechanical field variables and lower case letters will be used to denote meso-scale mechanical field variables.

2. Material and experimental method

In a recent work involving the authors [22], a series of in-situ neutron diffraction experiments were performed during biaxial loading of cruciform shaped samples of 316L stainless steel. In the following, we briefly recall the details of these tests that are relevant to this work.

2.1. Material properties

The material is a warm rolled face centered cubic (fcc) 316L stainless steel composed of: Cr-17.25, Ni-12.81, Mo-2.73, Mn-0.86, Si-0.53, C-0.02 (weight %). Electron backscattering diffraction (EBSD) analysis reveals a mild texture with an average grain size of ~7 μm. The mechanical properties of the material are tested using dog-bone samples prepared along the rolling and transverse direction. The mechanical response is similar for both type of samples, confirming a negligible role of the mild texture [22]. The von Mises (VM) stress v/s strain curve from a monotonic uniaxial tensile loading test is shown with a black line in Fig. 2.

2.2. Biaxial testing on cruciform sample geometry

Fig. 3 shows the cruciform geometry used in this work. Directions 1 and 2 in this figure represent the horizontal and vertical directions of the rig, respectively. All samples are prepared such that direction 1 is along the rolling direction. The sample has a circular gauge area of diameter 24 mm with a through thickness of 3 mm. Surface strains in the gauge area are measured in-situ using DIC. The biaxial tension, compression and torsion rig described in Ref. [22] is used to deform these cruciform shaped samples. Two types of monotonic loading are studied in this work: (a) uniaxial loading along the horizontal direction such that $F_2{:}F_1 = 0{:}1$, and (b) equibiaxial loading i.e. $F_2{:}F_1 = 1{:}1$. The results are compared with tensile loading tests on dog-bone samples [22]. All the tests are performed under load control at a rate of 40 N/s along each arm.

2.3. In-situ neutron diffraction

Neutron diffraction experiments were performed at the time-of-flight neutron strain scanner POLDI beamline located at the SINQ neutron facility of the Paul Scherrer Institut, Switzerland. Detailed information on the setup can be found in Refs. [33,34]. The incoming beam has a square cross-section with a side of 3.8 mm

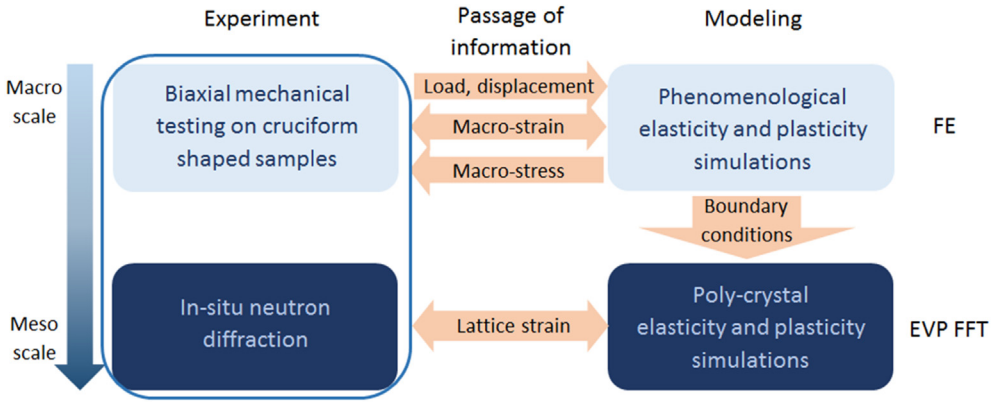

Fig. 1. Multi-scale synergetic combination of experiments and modeling to study in-situ diffraction during biaxial loading of cruciform samples. The arrows indicate passage of information within the multi-scale model, and between experiments and models.

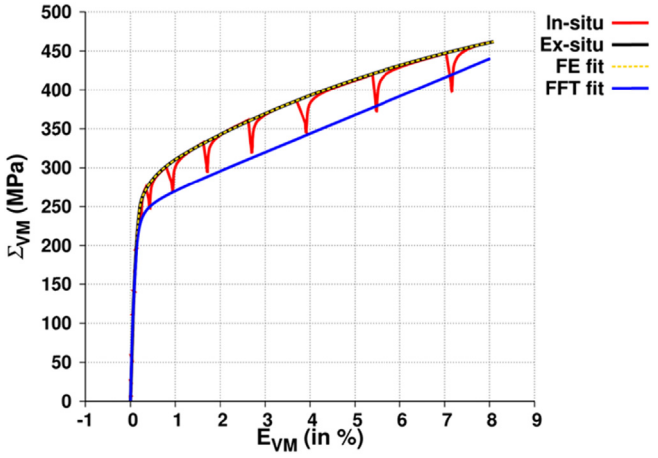

Fig. 2. VM stress v/s strain curve from uniaxial tensile loading on 316L stainless steel dog-bone samples. In red, the experimental curve obtained during in-situ neutron diffraction measurements. In black, the experimental curve during ex-situ monotonic loading. The dotted yellow line (overlapping the black line) is the macroscopic FE simulation fit, and the blue line is the EVPFFT fit. (For interpretation of the references to color in this figure legend, the reader is referred to the web version of this article.)

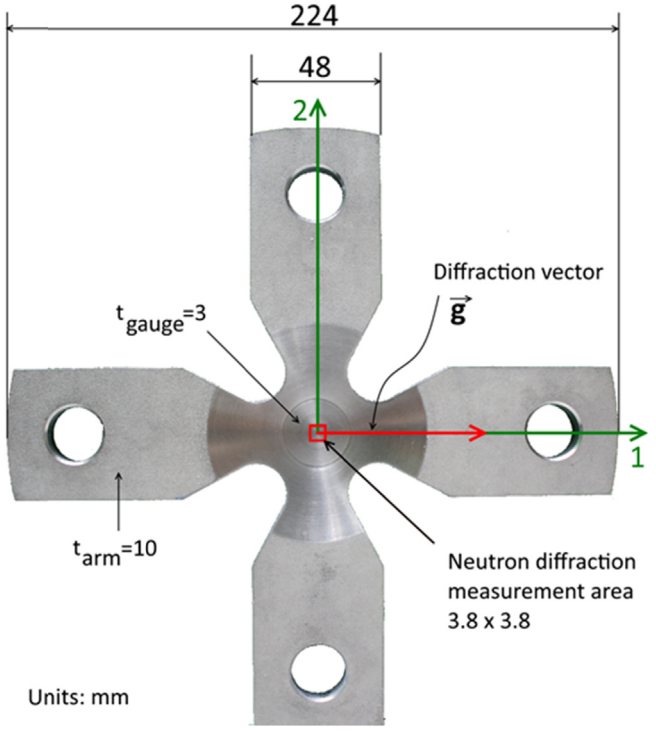

Fig. 3. Cruciform sample geometry used for biaxial deformation tests during in-situ neutron diffraction measurements.

and is incident at the centre of the circular gauge area. A single detector bank is installed at 90° relative to the incident beam. The samples are positioned at 45° to the incident and reflected beams such that the bisector of these beams i.e. the diffraction vector $\vec{g}$, lies along direction 1 of the cruciform sample (see Fig. 3). An *hkl* diffraction peak is obtained when the normal to the {*hkl*} planes (say $\vec{n}$) is closely aligned with $\vec{g}$. The detector has an angular acceptance range of $\Delta(2\theta) = \pm 15°$. This means that the detector measures all the grains that are oriented ±7.5° with respect to the in-plane direction. The data is analyzed with the POLDI standard single peak fitting procedure implemented in Mantid software [35].

The peak position of each *hkl* reflection determines the average inter-planar spacing d_{hkl} for a grain family with $\vec{n}$ parallel to $\vec{g}$. The average lattice strain for this grain family is then determined as the relative change in the average inter-planar spacing:

$$\varepsilon_{hkl} = \frac{d_{hkl} - d^0_{hkl}}{d^0_{hkl}} \quad (1)$$

where d^0_{hkl} is the initial average inter-planar spacing of the *hkl* grain family.

In-situ neutron measurements are taken at regular intervals during loading. Sample arms are held at constant displacement for the duration of the measurements. This results in stress relaxations in the gauge area. The red curve in Fig. 2 shows the VM stress v/s strain curve obtained from a uniaxial dog-bone test during in-situ neutron diffraction measurements. The neutron measurements are started after the initial sharp decrease in gauge stresses. For this steel, the waiting period before the neutron measurement was 2–3 min. Following this the neutron measurements are performed for 30 min. During the measurement period, the gauge stress decrease is negligible in comparison with the initial drop. Therefore, the stress state at which the diffraction peaks are measured corresponds to that of the cusps of the red curve in Fig. 2.

3. Multi-scale FE-FFT simulation setup

3.1. Macroscale FE simulations

ABAQUS/Standard software [31] is used to perform the FE simulations. In order to improve the computational efficiency, only 1/8th of the cruciform geometry is simulated. Symmetric boundary conditions are imposed on appropriate surfaces. A structured hexahedron mesh is employed with linear 8-node mesh elements (C3D8 in ABAQUS). Material properties of 316L stainless steel are assigned to the geometry. Due to its mild texture, the steel is assumed to be elastic isotropic macroscopically. The plastic response is modeled using the ABAQUS material model that is based on the von Mises (VM) yield criterion. The built-in combined non-linear isotropic and kinematic hardening law with 5 back-stresses is used. The stress v/s strain curve from the monotonic tensile loading test on dog-bone samples (black curve in Fig. 2) is provided as an input to ABAQUS/Standard. The ABAQUS/Standard algorithm uses this experimental curve to fit the back-stress parameters. Fig. 2 shows the VM stress v/s strain curve fitted by ABAQUS FE simulation (yellow dotted line). As can be seen, the fitted and experimental curves have a good match. Furthermore, the simulation results for stresses and strains are reproducible.

3.2. Meso-scale EVPFFT model

The full field EVPFFT approach [28] uses a periodic representative volume element (RVE) of the polycrystalline domain. The RVE is divided into evenly spaced voxels along the sample reference directions such that each grain contains several voxels. Single crystal elastic and plastic properties are attributed to each voxel. The elastic behavior of the material is modeled using Hooke's law and the viscoplastic behavior is modeled using a power law relationship [28,36] to mimic the evolution of a statistical ensemble of dislocations:

$$\sigma_{ij} = c_{ijkl}\varepsilon^{e}_{kl} \tag{2}$$

$$\dot{\gamma}^{s} = \sum_{s} \dot{\gamma}_0 \left(\frac{|m^{s}_{kl}\sigma_{kl}|}{\tau^{s}_{c}} \right)^{n} sgn(m^{s}_{kl}\sigma_{kl}) \tag{3}$$

$$\dot{\varepsilon}^{p}_{ij} = \sum_{s} m^{s}_{ij}\dot{\gamma}^{s} \tag{4}$$

where the tensor quantities σ_{ij}, c_{ijkl}, ε^{e}_{kl}, $\dot{\varepsilon}^{p}_{ij}$ and m^{s}_{kl} are the local stress, elastic stiffness, elastic strain, viscoplastic strain rate and Schmid tensor for slip system s, respectively. $\dot{\gamma}$, $\dot{\gamma}_0$, n and τ_s are the shear rate, reference shear rate, power law exponent and the critical resolved shear stress (CRSS) for the slip system s, respectively. The evolution of CRSS (τ^{s}_{c}) is modeled as a function of the total accumulated shear (Γ) on all slip systems using the extended Voce type hardening law [37]:

$$\tau^{s}_{c} = \tau^{s}_{0} + (\tau^{s}_{1} + \theta_1\Gamma)\left(1 - \exp\left(-\left|\frac{\theta^{s}_{0}}{\tau^{s}_{1}}\right|\Gamma\right)\right) \tag{5}$$

where τ_0, $(\tau_0 + \tau_1)$, θ_0 and θ_1 are the initial CRSS, the back extrapolated stress, the initial hardening slope and the final hardening slope for a given slip system, respectively. The increment in $\tau^{s}_{c}(\boldsymbol{x})$ is given as:

$$\Delta\tau^{s}_{c} = \frac{d\tau^{s}_{c}}{d\Gamma}\sum_{s\prime} h^{ss\prime}\Delta\gamma^{s\prime} \tag{6}$$

where $h^{ss\prime}$ is the hardening matrix with diagonal components corresponding to self-hardening coefficients and off-diagonal components correspond to latent hardening coefficients.

The numerical scheme is based on iteratively solving the stress equilibrium at each voxel in Fourier space under the action of macroscopic stress or strain rate boundary conditions. At the end of each time step, a compatible local total strain field is obtained that is constitutively related to an equilibrated local stress field. The FFT methodology ensures that the volume average of strain and stress fields at all voxels corresponds to the macroscopic stress and strain fields. A detailed explanation of the numerical approach for the infinitesimal strain EVPFFT approach is given in Refs. [28,29].

The simulated polycrystalline microstructure is constructed using Voronoi tessellations with 2500 grains. This microstructure is divided into 64 × 64 × 64 equi-spaced voxels along its reference directions. Two different initial textures are assigned for this microstructure (i) texture extracted from electron backscattering diffraction (EBSD) maps of as-received sample in Ref. [22] using the EDAX TEAM software, and (ii) randomly generated texture. Each voxel is assigned single crystal elastic properties for face centered cubic (fcc) 316L stainless steel obtained from Ref. [38]. The 3 independent elastic constants for this steel are $c_{11} = 204.6$ GPa, $c_{12} = 137.7$ GPa and $c_{44} = 126.2$ GPa and the corresponding elastic compliance constants are $s_{11} = 0.01066$ (GPa^{-1}), $s_{12} = -0.004288$ (GPa^{-1}) and $s_{44} = 0.007924$ (GPa^{-1}). This steel has a Zener anisotropic factor of $Z = \frac{2c_{44}}{c_{11}-c_{12}} = 3.77$. The plastic response is modeled using the rate-sensitive viscoplastic constitutive relationship in Eq. (6) assuming glide on the 12 {111}⟨110⟩ slip systems as the active slip mode and the viscoplastic exponent n = 35. The initial CRSS for each slip system of every voxel is taken to be the same. The Voce hardening parameters are fit to obtain an artificial stress–strain curve that joins all the cusps in Fig. 2. This is typically done in crystal plasticity modeling of in-situ diffraction experiments in order to capture the stress state encountered by the neutrons [24,27]. Table 1 shows the values of these parameters that fit the blue curve (Fig. 2) joining the points where in-situ neutron measurements are performed. All the self and latent hardening coefficients are assumed to be equal to 1.

3.3. Virtual diffraction

The polycrystalline sample reference frame is aligned such that the diffraction vector is along its (1,0,0) direction which is consistent with the cruciform loading direction 1. In the sample frame the *hkl* plane normal is given as $\vec{\boldsymbol{n}}^{sample} = \boldsymbol{R}\cdot\vec{\boldsymbol{n}}^{crystal}$; where $\boldsymbol{R}$ is the transformation matrix associated with the crystallographic orientation of the crystal at that voxel and $\vec{\boldsymbol{n}}^{crystal}$ is the *hkl* plane normal in the crystal reference frame. If $\vec{\boldsymbol{n}}^{sample}$ is nearly aligned with the diffraction vector $\vec{\boldsymbol{g}}$, then that voxel contributes to the *hkl* reflection. In accordance with the neutron diffraction experiment, an angular tolerance of ±7.5° between $\vec{\boldsymbol{n}}^{sample}$ and $\vec{\boldsymbol{g}}$ is used. The lattice strain at each voxel contributing to the *hkl* reflection is

Table 1
Voce hardening parameters for 316L stainless steel.

τ_0	τ_1	θ_0	θ_1
50 MPa	70 MPa	105000 MPa	410 MPa

computed as $\vec{g}\cdot\boldsymbol{\varepsilon}^{e}\cdot\vec{g}$. Its average over all contributing voxels $\langle\vec{g}\cdot\boldsymbol{\varepsilon}^{e}\cdot\vec{g}\rangle$ is then compared with the experimentally measured ε_{hkl} from Eq. (1). In this work, four *hkl* grain families are studied, namely, 111, 200, 220 and 311.

3.4. Passage of information between experiments and models

FE simulations are performed for the dog-bone and cruciform samples by linearly varying the forces in the arms from 0 to the maximum value applied during the experiments. The predicted total surface strains are averaged over the 3.8 mm × 3.8 mm central area and compared to the DIC strains obtained from the same area. If a good match is obtained, then the stress components are averaged over the 3.8 mm × 3.8 mm x 3 mm volume. These are then supplied as macroscopic stress boundary conditions to the EVPFFT model. The simulated microstructure deforms under the action of these stresses resulting in the generation of lattice strains at each voxel. The average of all the lattice strains over all the voxels belonging to the *hkl* grain family $\langle\vec{g}\cdot\boldsymbol{\varepsilon}^{e}\cdot\vec{g}\rangle$ is then compared with the average lattice strain ε_{hkl} in Eq. (1) obtained from *in-situ* neutron diffraction experiments.

4. Results

4.1. Macroscopic stress evolution in cruciform samples

Fig. 4a shows the FE predicted macroscopic surface strains E_{22} v/s E_{11} in comparison with the DIC measurements for uniaxial loading of a dog-bone sample, and uniaxial and equibiaxial loading of a cruciform sample. Simulation predicted and experimentally obtained strains have a good match for all three loadings. Minor differences between them may be due to the tolerances (range of 0.1 mm) associated with manufacturing the cruciform samples.

Fig. 4b shows the FE predicted macroscopic stress Σ_{22} as a function of Σ_{11} in the gauge region. Let R define the macroscopic stress ratio Σ_{22}/Σ_{11}. As can be expected, uniaxial loading in dog-bone samples results in a uniaxial stress state i.e. $R = 0$ and equibiaxial loading in cruciform samples results in an equibiaxial stress state i.e. $R = 1$. However, uniaxial loading in the cruciform sample results in a biaxial stress state in the gauge area. The cruciform geometry results in a coupling between the applied forces in the arms and the gauge stresses: $\Sigma_{11} = aF_1 - bF_2$ and $\Sigma_{22} = -bF_1 + aF_2$ [11–13]; where a and b are constant in the elastic regime and vary in the plastic regime. For the cruciform geometry shown in Fig. 3 (similar to those used in Refs. [12,13]) uniaxial load along direction 1 i.e. $F_2 = 0$, results in a compressive component along direction 2. Furthermore, the stress ratio R is −0.23 in the elastic regime and non-linearly changes to −0.37 during the elastic-plastic transition after which it remains constant until the end of loading. The origin and nature of this non-linear biaxial stress evolution will be studied in a separate work.

4.2. Role of macroscopic stresses on lattice strain evolution

The macroscale FE simulations for the cruciform samples also reveal that the out-of-plane normal stress Σ_{33} and all shear stress components Σ_{12}, Σ_{23} and Σ_{13} are negligibly small in comparison with in-plane biaxial stress components, during both uniaxial and equibiaxial loading. The maximum values of the norm of Σ_{12}, Σ_{23}, Σ_{13} and Σ_{33} attained during the entire course of loading are all less than 0.4% of the magnitude of Σ_{11} for both loadings. Consequently, the local mechanical behavior in the 3.8 × 3.8 × 3 mm^3 gauge region will be governed by the macroscopic stress ratio R. In the following the lattice strain analysis is performed as a function of the stress ratios (i) $R = 0$ (uniaxial dog-bone loading), (ii) $R = -0.23$ (elastic regime of uniaxial cruciform loading) varying continuously to −0.37 (plastic regime), and (iii) $R = 1$ (equibiaxial cruciform loading).

Fig. 5 shows the comparison between simulation predicted and experimentally measured [22] lattice strain evolution for the 200, 111, 220 and 311 grain families as a function of the macroscopic stress Σ_{11} for all load cases. Note that for the cruciform samples, the experimental lattice strains are plotted against the FE simulation predicted Σ_{11} generated by comparing the experimental lattice strain vs force in the arms to the FE simulation predicted stress vs force in the arms data; this procedure may contribute to the differences between the simulation predicted and experimental lattice strains for the cruciform samples. The simulations capture the experimental trends for the 200 grain family for all three loadings. The best match is obtained for $R = 0$ and corresponds well with the results presented in the work of Kanjarla et al. [39]. During uniaxial and equibiaxial loading in cruciform samples, the simulation predicted lattice strains for the 111 and 311 grain families match well the experimental ones in the elastic regime, however, they deviate away from each other in the plastic regime; the trend is captured for $R = -0.37$ but not for $R = 1$. Finally, for the 220 grain family,

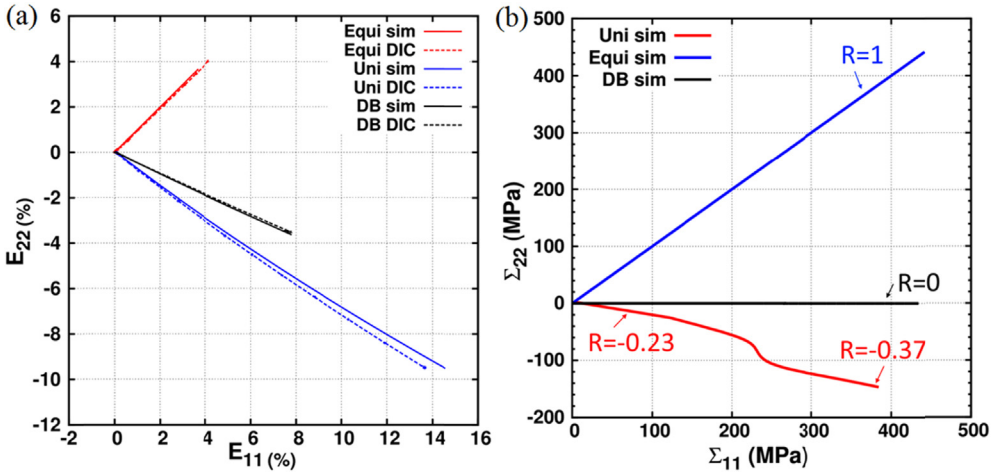

Fig. 4. FE simulation (sim) predicted evolution of (a) macroscopic surface strains compared with DIC measurements and (b) macroscopic stresses Σ_{22} vs Σ_{11} ($R = \Sigma_{22}/\Sigma_{11}$) for uniaxial (Uni) and equibiaxial (Equi) loading in cruciform samples in comparison with dog-bone (DB) samples.

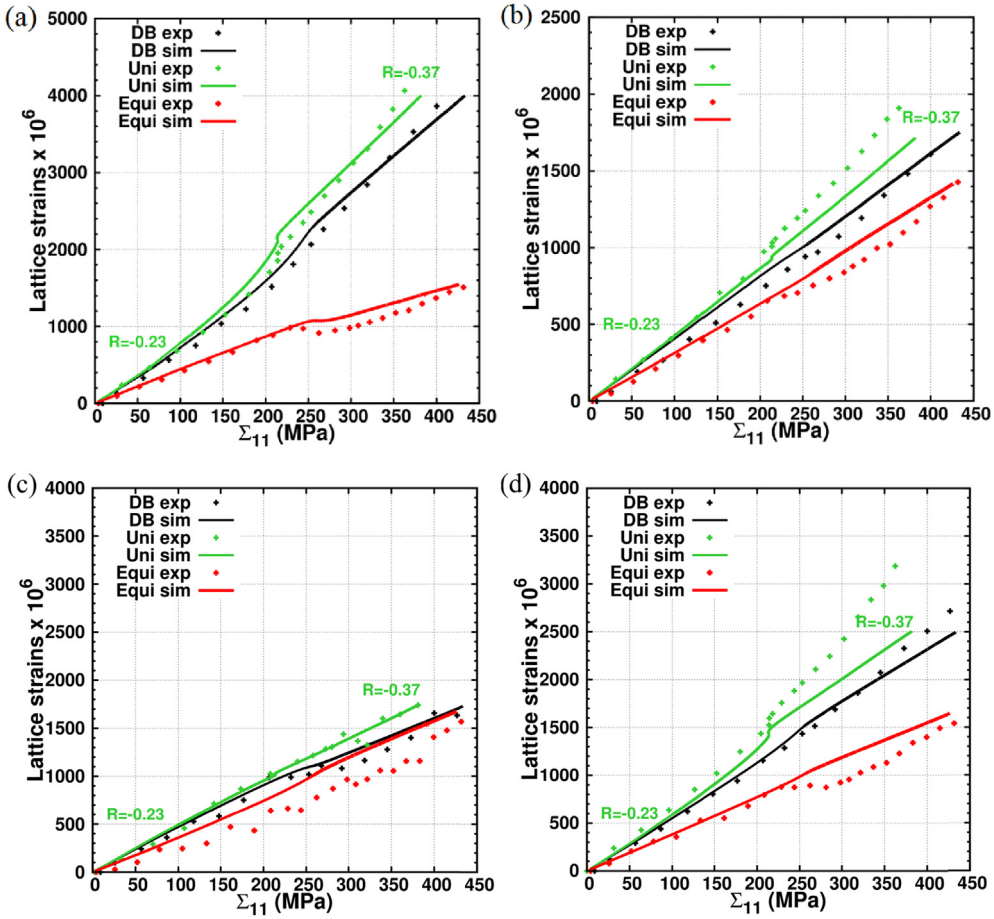

Fig. 5. Comparison between experimental and simulation predicted lattice strain evolution for (a) 200, (b) 111, (c) 220 and (d) 311 grain families for uniaxial loading in dog-bone sample (DB), and uniaxial (Uni) and equibiaxial (Equi) loading in cruciform samples as a function of Σ_{11}. The R values on the plots are associated with the green curve. (For interpretation of the references to color in this figure legend, the reader is referred to the web version of this article.)

there is a good match in the elastic regime for all three loadings and in the plastic regime for $R = 0$ and $R = -0.37$. The scatter in experimental data, which is especially important for equibiaxial loading, is due to a diminishing number of grains contributing to the 220 reflection reducing the intensity of this reflection [22]. This causes an increasing error on the peak profile fitting [35].

Simulations were also performed for a 3D microstructure derived from EBSD assuming equi-axed grains in the 3rd dimension. The 200 lattice strains from the EBSD microstructure have slightly larger deviations away from the experimental lattice strains during equibiaxial loading. Since the EBSD texture is a surface measurement and may not be representative of the overall texture, and since it only pointed towards a mild texture [22], all simulations are performed using the random RVE.

Uniaxial loading in the cruciform sample results in the most compliant lattice strain response for all grain families. A distinctive kink in the lattice strain evolution of all grain families is observed during the elastic-plastic transition regime where R changes from -0.23 to -0.37. Furthermore, for all grain families this kink occurs in the same direction. Note here that because macroscopic plasticity is governed by the VM yield criterion, $R = -0.23$ causes yielding at a lower Σ_{11} in comparison to that for $R = 0$ or $R = 1$. Stress ratio $R = 1$ results in the stiffest lattice strain response in the elastic regime. During the elastic-plastic transition, the lattice strain evolution under $R = 1$ deviates towards that of $R = 0$ for the 220 family and away for the 111, 200 and 311 families. At the end of loading, $R = 0$ and $R = 1$ result in nearly equal lattice strain in the 220 family and have a large difference for the remaining families.

Fig. 6 shows the comparison of lattice strain per grain family for 200, 111, 220 and 311 reflections and the macroscopic elastic strain E^e_{11} as a function of Σ_{11} for the three loading cases. Note that the evolution of E^e_{11} is representative of the average lattice strain response of the polycrystalline aggregate along the diffraction measurement direction in the absence of shear components. For clarity, only the simulation results are shown. Under $R = 0$, the elastic anisotropy of 316L stainless steel along with elastic interactions with the grain neighborhood causes the observed lattice strain spread in the elastic regime [39,40]. In the plastic regime, the variation in spread is due to a combination of the elastic anisotropy, elastic interactions with grain neighborhood, plastic slip and plastic interactions with grain neighborhood. Under a biaxial load, the lattice strain response has an additional dependence on the ratio R. During uniaxial loading in cruciform samples, the change from $R = -0.23$ and -0.37 results in different magnitudes of kinks for different grain families; the magnitude of the kink is the highest for the 200 family and the lowest for the 111 family. Since all the kinks are in the same direction, this results in a larger spread in the lattice strain evolution in comparison with the spread in lattice strain under $R = 0$. Under uniaxial loading in both dog-bone and cruciform samples, in the elastic and plastic regimes the 200 grain family has the most compliant response. Meanwhile the 111 family has the stiffest response in the elastic regime and the 220 family has a stiffer response in the plastic regime. This results in the same

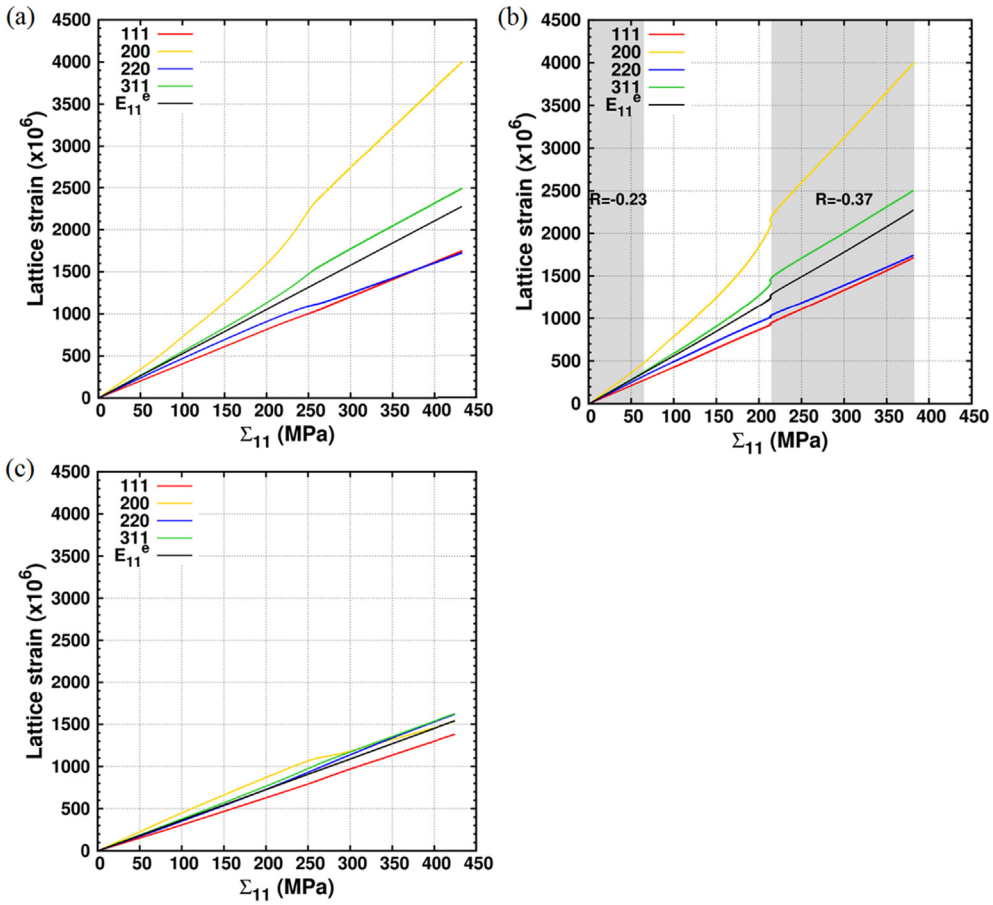

Fig. 6. Lattice strain evolution in the 111, 200, 220 and 311 grain families and the macroscopic elastic strain E^e_{11} from FE simulations as a function of Σ_{11} for (a) $R = 0$ (b) $R = -0.23$ and -0.37, and (c) $R = 1$.

lattice strain magnitude in both 220 and 111 families at the end of loading. Furthermore, in accordance with the existing literature, the lattice strain evolution in the 311 family is representative of the macroscopic elastic response for $R = 0$ [20,40,41]. Fig. 6 shows that this is also true for uniaxial loading in cruciform samples.

The spread in lattice strain evolution is significantly smaller for $R = 1$. In the elastic regime, the 200 and 111 grain families are the stiffest and the most compliant, respectively, but only by a small margin. At the end of loading, however, the 220 and 311 have the most compliant response. Due to the narrowness of the spread in lattice strains, it is difficult to isolate a single grain family that follows the macroscopic elastic response during the entire course of loading. In this case, the lattice strain evolution in any grain family may be taken as representative of the macroscopic behavior.

In the following section, a detailed quantitative analysis is performed on the 200 and 220 grain families to understand the role of R on their lattice strain response in the elastic and plastic regimes.

5. Discussion

A grain family constituting an *hkl* reflection has the cruciform loading direction 1 normal to one of its {*hkl*} set of planes and the loading direction 2 contained in that plane. This *hkl* grain family can be divided into sub-sets of grains according to the alignment of loading direction 2 with an in-plane direction. This is illustrated in Fig. 7a for the 200 grain family. The gauge region of the cruciform samples from Fig. 3 is used to show the crystallographic orientation of three grains of the 200 grain family. Loading direction 1 is parallel to the normal to {200} planes and loading direction 2 is parallel to the in-plane directions: 010, 031 and 011. These in-plane directions can be comprised in a set of $\langle a_i b_i c_i \rangle$ directions. Under the action of a stress ratio $R \neq 0$, the lattice strain response of different $hkl\langle a_i b_i c_i \rangle$ sub-sets of the *hkl* family will depend on (a) the ratio R, (b) elastic anisotropy, (c) resolved shear stress on each slip system and (d) elastic and plastic interactions with the grain neighborhood. In order to understand the lattice strain evolution of different grain families, it is crucial to understand the lattice strain evolution within each grain family. In this section, the analysis is performed on the sub-sets of 200 and 220 families These show the most interesting trends in the lattice strain evolution.

All grains contributing to the 200 reflection have one of their crystal reference direction parallel to the $\langle 200 \rangle$ direction and the other two directions are in the {200} plane. On an inverse pole figure the possible crystallographic direction in that plane lie within the region bounded by the $\langle 010 \rangle$ and $\langle 011 \rangle$ directions as shown in Fig. 7b. Because the detector has an angular range of $\pm 7.5^\circ$, all grain within this range will contribute to the 200 reflection. In what follows, we consider the grain sub-sets $200\langle 010 \rangle$, $200\langle 031 \rangle$, $200\langle 021 \rangle$ and $200200\langle 011 \rangle$. Similarly, for the {200} family, one of the crystal reference directions is parallel to the $\langle 220 \rangle$ direction and the other two lie in the {220} plane between the set of directions $\langle 001 \rangle$ and $\langle 1\bar{1}0 \rangle$. The grain sub-sets $220\langle 001 \rangle$, $220\langle 1\bar{1}3 \rangle$, $220\langle 1\bar{1}1 \rangle$, $220\langle 3\bar{3}1 \rangle$ and $220\langle 1\bar{1}0 \rangle$ will be considered. On an inverse

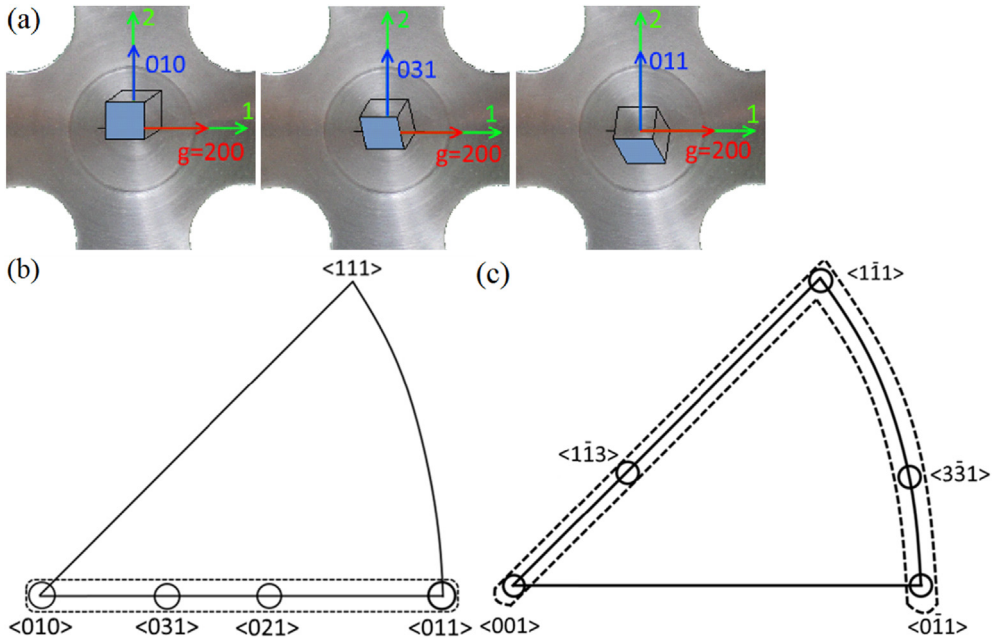

Fig. 7. (a) 200 reflection and loading directions in crystal reference frame. The ⟨010⟩ inverse pole figure showing the range of $hkl\langle a_i b_i c_i\rangle$ sub-sets belonging to the (b) 200 and (c) 220 reflections.

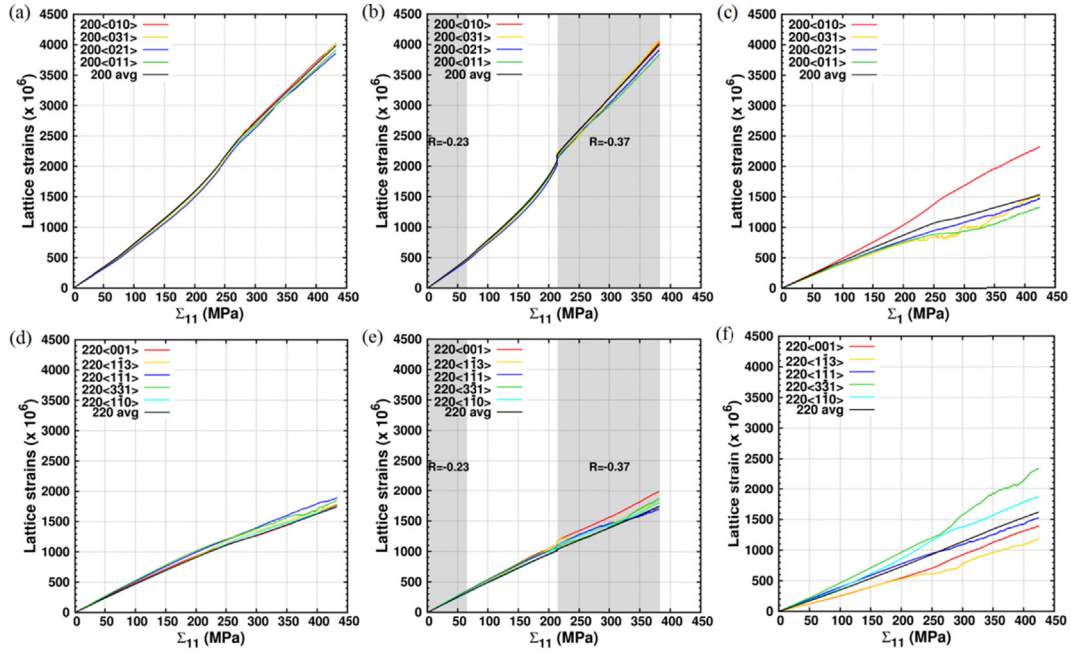

Fig. 8. Lattice strain evolution in the (a, b, c) 200 grain and its subsets and (d, e, f) 220 grain and its subsets for (a, d) uniaxial dog-bone, (b, e) uniaxial cruciform and (c, f) equibiaxial cruciform loading.

pole figure these lie in the region within the dotted lines in Fig. 7c. Fig. 8 shows the lattice strain evolution of the sub-sets of 200 and 220 grains for the three load cases.

5.1. Load dependence in the elastic regime

We first consider the elastic compliance of single crystals subjected to R. Under the action of a macroscopic uniaxial stress $R = 0$ perpendicular to the (hkl) plane, the directional elastic compliance of each sub-set $s_{hkl[a_i b_i c_i]} = \varepsilon_{hkl}/\Sigma_{11}$ is the same for an hkl crystal [42]. From Eqs. (A.18) and (A.19) in the Appendix, the directional elastic compliances of 200 and 220 single crystals for $R = 0$ are $s_{200[a_i b_i c_i]} = s_{11}$ and $s_{220[a_i b_i c_i]} = s_{11} - \frac{1}{2}\left(s_{11} - s_{12} - \frac{s_{44}}{2}\right)$, respectively; the notations are described in the Appendix. Since these values are independent of the orientation within the (200) and (220) planes, no sub-grain sets have to be considered.

When a single crystal is subjected to $R \neq 0$, the directional elastic compliance becomes dependent on R and in some cases on the direction $[a_i b_i c_i]$ contained in the (hkl) plane. For the 200 and

Table 2
Analytically computed ($\times 10^{-3}$ GPa^{-1}) single crystal (SC) $s_{hkl[a_ib_ic_i]}$, and the percentage difference simulation predicted polycrystalline (PC) $s_{hkl\langle a_ib_ic_i\rangle}$ at $\Sigma_{11} = 50$ MPa and single crystal $s_{hkl[a_ib_ic_i]}$ for sub-sets of 200 and 220 single crystals of 316L stainless steel as a function of the stress ratio R. In round brackets are the $s^{isotropic}_{hkl[a_ib_ic_i]}$ for a single crystal with isotropic elastic properties.

	$R = 0$		$R = -0.23$		$R = 1$	
	SC	PC	SC	PC	SC	PC
200⟨010⟩	10.66 (5.26)	−34.99	11.65 (5.64)	−37.42	6.37 (3.62)	−25.59
200⟨031⟩		−39.87		−41.89		−36.11
200⟨021⟩		−40.71		−42.83		−33.75
200⟨011⟩		−37.34		−39.23		−33.12
220⟨001⟩	5.17 (5.26)	−3.87	6.15 (5.64)	−12.68	0.88 (3.62)	187.5
220⟨1$\bar{1}$3⟩		−10.44	5.92 (5.64)	−16.22	1.88 (3.62)	38.30
220⟨1$\bar{1}$1⟩		0.77	5.31 (5.64)	1.89	4.54 (3.62)	−12.11
220⟨3$\bar{3}$1⟩		4.06	4.96 (5.64)	11.49	6.08 (3.62)	−26.32
220⟨1$\bar{1}$0⟩		−9.67	4.89 (5.64)	−1.02	6.37 (3.62)	−42.54

220 single crystals, the directional elastic compliances (see Eqs. (A.22) and (A.23)) are, respectively, $s_{200[a_ib_ic_i]} = s_{11} + Rs_{12}$ and $s_{220[a_ib_ic_i]} = s_{11} + Rs_{12} + \frac{1}{2}\left(s_{11} - s_{12} - \frac{s_{44}}{2}\right)\left[(1 - w_i^2)R - 1\right]$; here $w_i = \frac{c_i}{\sqrt{a_i^2+b_i^2+c_i^2}}$ is a direction cosine of $[a_ib_ic_i]$. Table 2 shows the single crystalline $s_{200[a_ib_ic_i]}$ and $s_{220[a_ib_ic_i]}$ as a function of R for 316L stainless steel. Similar to $R = 0$, $s_{200[a_ib_ic_i]}$ is independent of the crystal orientation in the (200) plane. From Eq. (A.24), this is also the case for sub-sets of 111 single crystals. In contrast, $s_{220[a_ib_ic_i]}$ is now dependent on the crystal orientation in the (220) plane. In addition, the contribution of the crystal orientation is weighed according to the value of R. The higher the absolute value of R, the larger is the spread in $s_{220[a_ib_ic_i]}$ between the different sub-sets. Furthermore, for $R = -0.23$, the 220[001] family is the most compliant and the 220[1$\bar{1}$0] is the stiffest which is contrary to the trend for $R = 1$. Therefore, the differences in $s_{220[a_ib_ic_i]}$ are also dependent on the sign of the stress ratio R. From Eq. (A.25) this is also found to be the case for 311 single crystals.

In order to understand the contribution of elastic anisotropy, we set the single crystal elastic compliance components using their isotropic estimates as $s_{11} = \frac{1}{E}$, $s_{12} = -\frac{\nu}{E}$ and $s_{44} = \frac{2(1+\nu)}{E}$. Similar to the work of Oliver et al. [43], the Young's modulus (E) and Poisson's ratio (ν) are assigned their experimentally measured macroscopic values. The corresponding $s^{isotropic}_{hkl[a_ib_ic_i]}$ for the 200 and 220 isotropic elastic crystals are shown in Table 2 in round brackets. For the 200 sub-sets, the $s^{isotropic}_{200[a_ib_ic_i]}$ are approximately half in magnitude of their anisotropic counterparts for all R. For the 220 sub-sets, the $s_{220[a_ib_ic_i]}$ and $s^{isotropic}_{220[a_ib_ic_i]}$ are very similar for $R = 0$. For $R \neq 0$, the $s_{220[a_ib_ic_i]}$ are scattered about $s^{isotropic}_{220[a_ib_ic_i]}$. For $R = -0.23$, $s_{220[001]}$ and $s_{220[1\bar{1}3]}$ are higher in magnitude than their isotropic counterparts. Whereas $s_{220[1\bar{1}1]}$, $s_{220[1\bar{1}3]}$ and $s_{220[1\bar{1}0]}$ are lower in magnitude than their isotropic counterparts. These trends are reversed for $R = 1$. Note that due to the imposed elastic isotropy, the term $\left(s_{11} - s_{12} - \frac{s_{44}}{2}\right)$ becomes equal to 0. Therefore, $s^{isotropic}_{220[a_ib_ic_i]}$ has the same magnitude as $s^{isotropic}_{200[a_ib_ic_i]}$ for a given R. This implies that the crystal orientation in the (hkl) plane only contributes to the $s_{hkl[a_ib_ic_i]}$ when the crystal is elastically anisotropic and $R \neq 0$.

In the polycrystalline case, the magnitudes of $s_{hkl[a_ib_ic_i]}$ are strongly influenced by the grain neighborhood interactions along with the load distributions between different families. Table 2 also shows the percentage difference between simulation predicted polycrystalline $s_{hkl\langle a_ib_ic_i\rangle}$ and single crystal $s_{hkl[a_ib_ic_i]}$ for 200 and 220 family sub-sets as a function of the stress ratio R. The percentage difference between $s_{200\langle a_ib_ic_i\rangle}$ and $s_{200[a_ib_ic_i]}$ is significantly large for $R = 0$. It further increases for $R = -0.23$, and decreases for $R = 1$. In general, the $s_{200\langle a_ib_ic_i\rangle}$ is stiffer than $s_{200[a_ib_ic_i]}$ for all R. The percentage difference between $s_{220\langle a_ib_ic_i\rangle}$ and $s_{220[a_ib_ic_i]}$ is small for $R = 0$. It increases slightly for $R = -0.23$ and significantly for $R = 1$. This is in contrast to the percentage differences between $s_{200\langle a_ib_ic_i\rangle}$ and $s_{200[a_ib_ic_i]}$. Furthermore, the 220⟨001⟩ and 220⟨1$\bar{1}$3⟩ sub-sets become increasingly stiffer than their single crystal counterparts as R decreases from 0 to −0.23, and increasingly more compliant as R increases from 0 to 1. The trend is vice versa for the 220⟨1$\bar{1}$1⟩, 220⟨3$\bar{3}$1⟩ and 220⟨1$\bar{1}$0⟩ sub-sets. The deviations in $s_{hkl[a_ib_ic_i]}$ will vary differently for different grain morphologies and texture and therefore a trend on the influence of grain neighborhood interactions on lattice strain evolution is not evident.

Table 3 shows the analytical single crystal and simulation predicted polycrystalline directional elastic compliance averaged over all sub-sets for each grain family i.e. s_{hkl} as a function of R; for the 311 grain family, the analytical single crystal s_{311} is computed considering the subsets 311[01$\bar{1}$], 311[31$\bar{1}\bar{1}$0], 311[1$\bar{3}$0], 311[$\bar{1}$12] and 311[$\bar{2}$33]. For a given R, the ordering of grain families from the most compliant to the stiffest is 200, 311, 220 and 111 for both single and polycrystalline microstructures. The polycrystalline s_{hkl} for the 200, 311 and 220 families is higher in magnitude than its single crystalline counterpart for all R. Surprisingly, the trend is opposite for the 111 family. For both single crystal and polycrystalline cases, the spread in s_{hkl} between the different grain families decreases as R increases from −0.23 to 1. Interestingly, this is in contrast to the spread in $s_{hkl\langle a_ib_ic_i\rangle}$ as a function of R between the sub-sets of a given hkl family. Furthermore, the spread in s_{hkl} is larger in the single crystalline case in comparison with the polycrystalline case for all R. In the polycrystalline case, s_{hkl} is affected by the grain neighborhood interactions of each grain in every sub-set belonging to the hkl grain family. The magnitude of s_{hkl} is a weighted average of $s_{hkl\langle a_ib_ic_i\rangle}$ over all the voxels belonging to each

Table 3
Analytically computed (x10^{-3} GPa^{-1}) single crystal (SC) and simulation predicted polycrystalline (PC) directional elastic compliance s_{hkl} for 200, 220, 111 and 311 grain families as a function of the stress ratio R.

	$R = 0$		$R = -0.23$		$R = 1$	
	SC	PC	SC	PC	SC	PC
200	10.66	6.84	11.65	7.22	6.37	4.51
220	5.17	4.76	5.45	4.97	3.95	3.46
111	3.34	4.05	3.48	4.22	2.71	3.05
311	7.21	5.40	7.77	5.68	4.77	3.75

hkl sub-set. The combination of these along with load sharing between different grain families determines their lattice strain evolution in the elastic regime.

5.2. Load dependence in the plastic regime

The resolved shear stress (RSS) per slip system, τ^s, is determined from the local stress state at each voxel according to the Schmid law ($\tau^s = m^s_{kl}\sigma_{kl}$). In the elastic regime, the evolution of τ^s depends on R, the elastic anisotropy and elastic grain neighborhood interactions. Consequently, the onset of plasticity is influenced by these factors. Following the onset of plasticity, the evolution of τ^s has an additional dependence on the local crystallographic orientations and grain neighborhood interactions due to plastic anisotropy. Through the power law in Eq. (3), τ^s determines the plastic shear rate at every voxel, consequently increasing the accumulated plastic strain at that voxel. As a result, the lattice strain evolution is directly affected by the evolution of τ^s.

Focusing on the 200 family, at $R = 0$ eight slip systems with equal τ^s are activated in all the 200 sub-sets. This is illustrated in Fig. 9a, c and e for the 200[010], 200[021] and 200[011] single crystals using a 2-dimensional representation of the Thompson's tetrahedron. For this loading, the orientation of the crystal normal to the uniaxial loading direction does not affect the slip activity. Consequently, the lattice strains of each 200 sub-set evolve in the same way as confirmed in Fig. 8a. As R deviates away from 0, the slip activity in these sub-sets begins to differ with respect to (i) number of active slip systems, (ii) their type and (iii) their τ^s. The differences in slip activity between different 200 sub-sets is maximum at $R = 1$. For instance, in the 200[010] single crystal eight slip systems are active but some of them are on different planes compared to those at $R = 0$ (see Fig. 9a and b). Furthermore, in Fig. 9a all the arrowheads are pointing towards the X-direction with four each pointing away from Y and Z directions. Therefore, under $R = 0$ the slip activity results in a tensile plastic strain along the X-direction that is two times larger than the compressive plastic strain along the Y and Z directions. Whereas, in Fig. 9b all the arrow heads are pointing away from the Z-direction with four each pointing towards X and Y directions. This implies that the compressive plastic strain along the Z-direction is two times the tensile plastic strain along X and Y. On the other hand, the 200[011] sub-set has only four active slip systems having the same τ^s (see Fig. 9d). In the 200[021] sub-set, two slips systems have the highest τ^s. Whereas six other slip systems have half the magnitudes of the highest τ^s and two slip systems can be found with, respectively, one third and one sixth of the maximum value. Since all slip systems

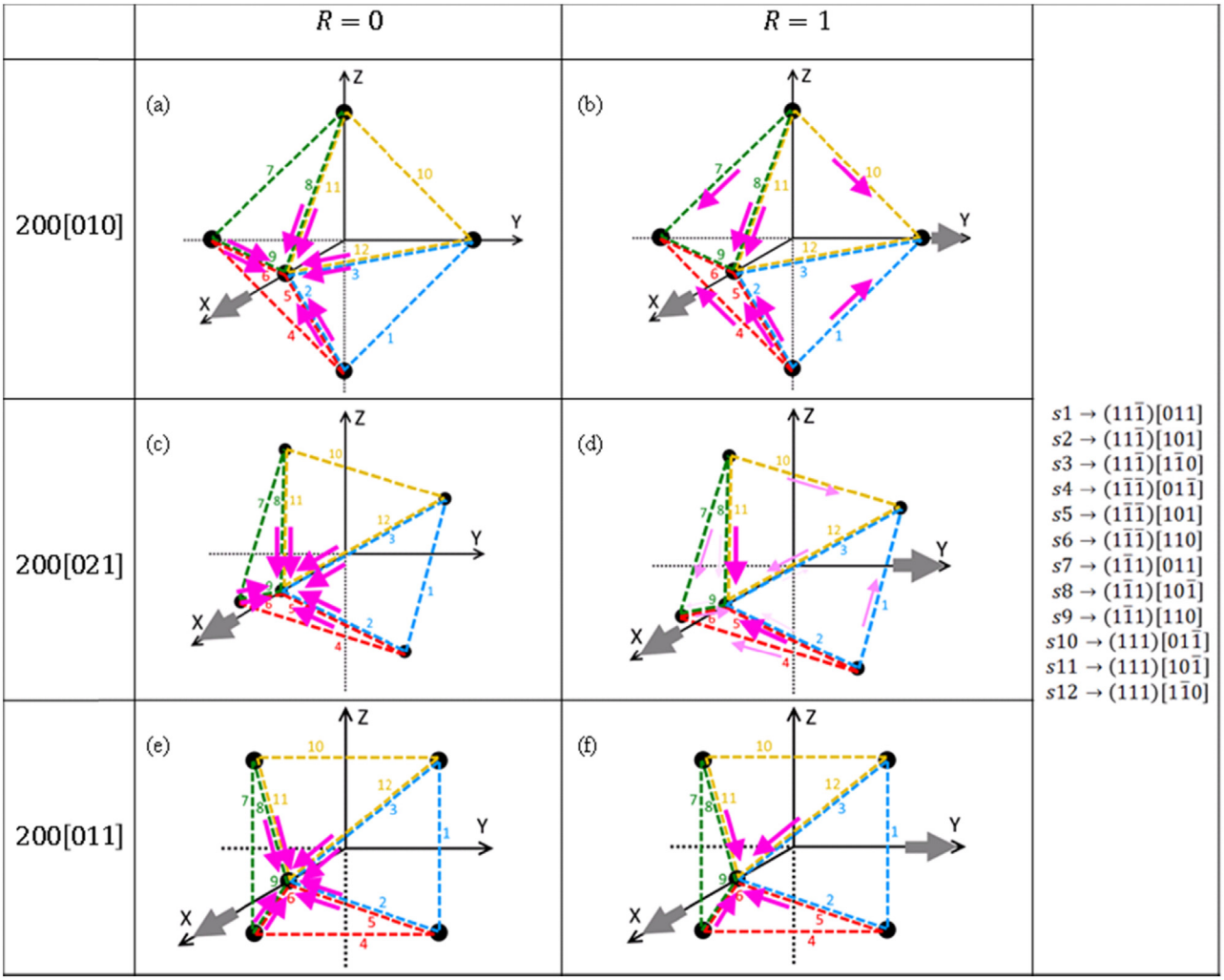

Fig. 9. Distribution of τ^s on different slip systems for the (a, b) 200[010], (c, d) 200[021] and (e, f) 200[011] single crystals under (a, c, e) $R = 0$ and (b, d, f) $R = 1$. The arrow head size and color density of the pink arrows represents the relative magnitude of τ^s (not to scale). (For interpretation of the references to color in this figure legend, the reader is referred to the web version of this article.)

harden equally (latent and self-hardening coefficients are 1) and the power law exponent in Eq. (3) is 35, only two slip systems with the highest τ^s are active. The same is true for the 200[031] sub-set.

To highlight the role of the different active slip systems on the lattice strain evolution, single crystal simulations are performed for 200[010], 200[021] and 200[011] crystals subjected to $R = 1$. Note here that these simulations do not account for intra-granular stress variations due to elastic heterogeneity or grain neighborhood interactions. Results show that for any given applied Σ_{11}, the RSS of the 8 active slip systems in the 200[010] crystal is always equal to the RSS of the 4 active slip systems of 200[011] crystal. For the same Σ_{11} the 2 active slip systems in the 200[021] crystal always have a higher RSS than in the two other crystals. Consequently, plasticity initiates first in the 200[021] crystal. At the on-set of plasticity in 200[010] and 200[011] crystals, the shear rates $\dot{\gamma}^s$ per active slip system for both these crystals are the same. The shear rates in the 200[011] crystal then rapidly increase to become two times the shear rates in the 200[010] crystal. At the same time, the shear rates of active slip systems in the 200[021] crystal are more than two times larger than the values in the 200[011] crystal. Meanwhile, the lattice strains along the 200 direction for all three crystals have the same magnitudes at all stages of loading. These results imply that in order to maintain the same lattice strain evolution under the same applied stress state, $\dot{\gamma}^s$ in 200[021] crystals should be more than two times and four times larger than in the 200[011] and 200[010] crystals, respectively.

In the polycrystalline case, shear activity in one of the 200 sub-sets results in a partial load transfer to other 200 sub-sets or grain families. This is reflected in the evolution of τ^s, $\dot{\gamma}^s$ and consequently the lattice strains. However, following the evolution of τ^s and $\dot{\gamma}^s$ in every slip system of every voxel belonging to the 200 sub-set is impracticable. Furthermore, the *hkl* multiplicity implies that within the same sub-set two grains may have different types of active slip systems. Therefore, we compute the L^1-norm of τ^s averaged over all the slip systems in all the voxels (that satisfy diffracting conditions) belonging to each 200 sub-sets i.e. $\langle \sum_s |\tau^s| \rangle = \frac{1}{12 N_{200\langle u_i v_i w_i \rangle}} \sum_{N_{200\langle u_i v_i w_i \rangle}} \sum_s |\tau^s|$; where $N_{200\langle u_i v_i w_i \rangle}$ is the number of voxels in diffracting conditions belonging to the $200\langle u_i v_i w_i \rangle$ sub-sets. This expression accounts for the multiplicity of grains belonging to each sub-set. Note that the averaging procedure for $\langle \sum_s |\tau^s| \rangle$ lowers the τ^s threshold for the on-set of plasticity below the CRSS. In order to clearly understand the load transfer due to plasticity, $\langle \sum_s |\tau^s| \rangle$ normalized with respect to Σ_{11} i.e. $\frac{\langle \sum_s |\tau^s| \rangle}{\Sigma_{11}}$ is plotted as a function of Σ_{11} in Fig. 10a. This ratio is denoted as *NARSS* (normalized average *RSS*) $= \frac{\langle \sum_s |\tau^s| \rangle}{\Sigma_{11}}$. Fig. 11 shows the L^1-norm of $\dot{\gamma}^s$ averaged over all the slip systems in all the voxels contributing to each 200 sub-sets i.e. $\langle \sum_s |\dot{\gamma}^s| \rangle$ is plotted as a function of Σ_{11}.

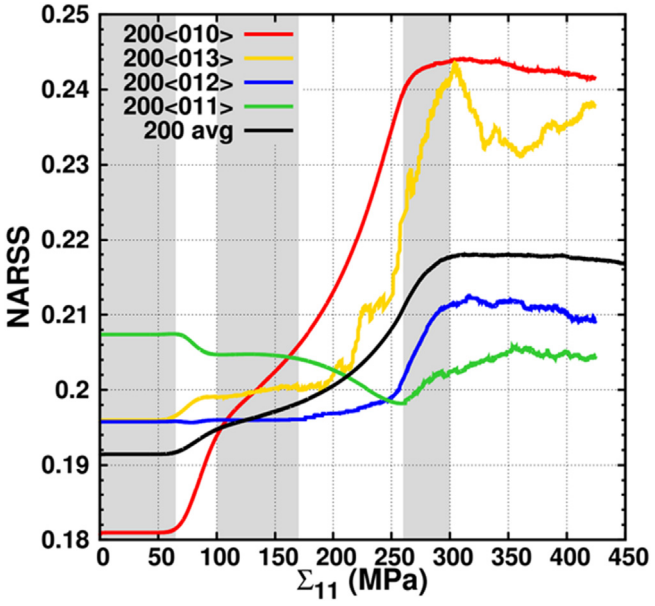

Fig. 10. *NARSS* plotted as a function of Σ_{11} for the 200 family and its sub-sets subjected to $R = 1$. The grey and white rectangles represent different regions where *NARSS* shows interesting changes in evolution.

Prior to the onset of plasticity, *NARSS* is highest for $200\langle 011 \rangle$ sub-set, has equal intermediate values for $200\langle 021 \rangle$ and $200\langle 031 \rangle$ sub-sets, and the lowest value for the $200\langle 010 \rangle$ sub-set. At the on-set of plasticity where $\Sigma_{11} = 65$ MPa, the $200\langle 011 \rangle$ sub-set begins to deform plastically and sheds part of its load. This causes a decrease in *NARSS*. At the same time, *NARSS* increases with an equal amount in the $200\langle 031 \rangle$ sub-set. This causes the $200\langle 031 \rangle$ sub-set to begin deforming plastically. From $\Sigma_{11} = 85$ MPa to 100 MPa, the $200\langle 031 \rangle$ sheds this extra load resulting in no change in *NARSS* near $\Sigma_{11} = 100$ MPa. The $200\langle 011 \rangle$ sub-set also reaches a constant value for *NARSS* near $\Sigma_{11} = 100$ MPa. This is directly reflected through the slower lattice strain increment rate in the $200\langle 031 \rangle$ and the $200\langle 011 \rangle$ sub-sets in Fig. 8c. During this time, the $200\langle 021 \rangle$ sub-set continues to take the same load as in the elastic regime resulting in no change in *NARSS* and the lattice strain increment rate. From the on-set of plasticity to $\Sigma_{11} = 100$ MPa, the $200\langle 010 \rangle$ sub-set takes increasingly higher load causing a steep increase in *NARSS*. However, these sub-sets begin to deform plastically only at $\Sigma_{11} = 80$ MPa with a rate that is less than half of the other sub-sets. Consequently, the lattice strain increment rate in $200\langle 010 \rangle$ is increasingly faster than in the elastic regime. The combined effect of all these sub-sets is a slightly faster increase in *NARSS* and lattice strains of the 200 family. This implies that the 200 family has transferred a part of the load from other grain families.

Between $\Sigma_{11} = 100$ MPa and 170 MPa, there is very little change in *NARSS* for the $200\langle 031 \rangle$, the $200\langle 021 \rangle$ and the $200\langle 011 \rangle$ sub-sets. The $200\langle 010 \rangle$ sub-set continues to have an increasing *NARSS*, however at a slower rate. At $\Sigma_{11} = 100$ MPa, the $200\langle 010 \rangle$ sub-set takes the highest value for *NARSS* followed by $200\langle 010 \rangle$, $200\langle 031 \rangle$ and $200\langle 021 \rangle$. However, this does not result in a significant change in the lattice strain evolution. From $\Sigma_{11} = 170$ MPa to 260 MPa, the $200\langle 011 \rangle$ sub-set sheds its load again resulting in an increasingly faster decrease in *NARSS*. Consequently, the lattice strain increment rate becomes slower. However, *NARSS* begins to increase in the $200\langle 031 \rangle$ and $200\langle 021 \rangle$ sub-sets causing an increase in $\langle \sum_s |\dot{\gamma}^s| \rangle$. This results in a slower lattice strain increment rate for these sub-sets. Meanwhile, the $200\langle 010 \rangle$ sub-set and the 200 family continue to have an increasing *NARSS* but now at a faster rate than between $\Sigma_{11} = 100$ MPa to 170 MPa.

At $\Sigma_{11} \approx 260$ MPa, the lattice strain evolution of the $200\langle 031 \rangle$ sub-set becomes very noisy. This is because a significant number of voxels belonging to this sub-set have moved out of diffracting conditions in comparison with the onset of plasticity. This is due to local plastic rotations resulting from slip activity. The jumps observed in $\langle \sum_s |\dot{\gamma}^s| \rangle$ are due to the differences in local shear rates between the few separated voxels that move in and/or out of diffracting conditions. This makes it difficult to meaningfully describe the behavior of the $200\langle 031 \rangle$ sub-set. At $\Sigma_{11} = 260$ MPa, the $200\langle 010 \rangle$ sub-set begins to plastically deform faster than the other grain-subsets. This causes a slower rate of lattice strain increment in the $200\langle 010 \rangle$ sub-set. As a consequence, a significant part of its

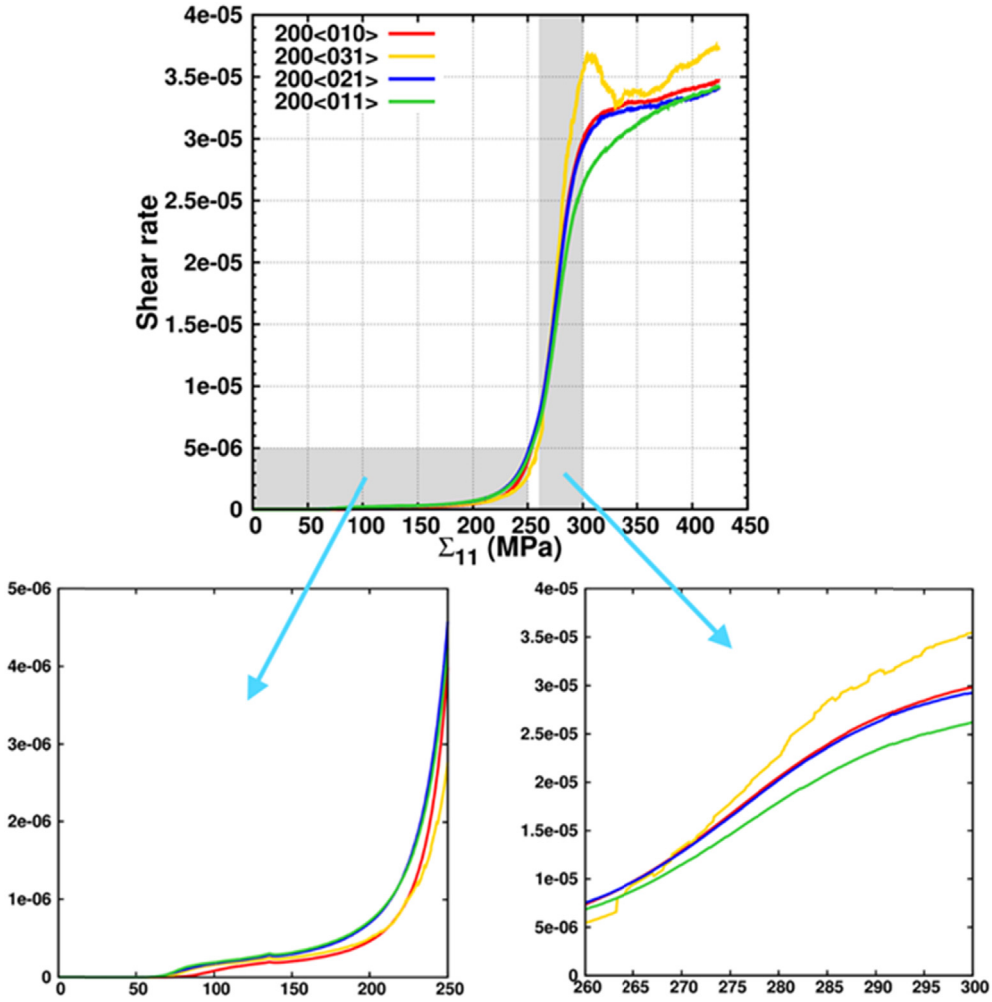

Fig. 11. $\langle\sum_s|\dot{\gamma}^s|\rangle$ plotted as a function of Σ_{11} for the 200 family sub-sets subjected to $R = 1$. The grey rectangles indicate the two zoomed in regions.

load is transferred to the 200⟨031⟩, 200⟨021⟩ and 200⟨011⟩ sub-sets, and other grain families resulting in an increase of $\langle\sum_s|\dot{\gamma}^s|\rangle$ for the 200⟨021⟩ and 200⟨011⟩ sub-sets. This in turn causes a slower lattice strain increment rate for these sub-sets. The combined effect of these is a slower rate of lattice strain increment within the 200 family. This implies that the 200 family transfers a part of its load to other grain families. Furthermore, this explains the significant increase in the spread in directional elastic compliance $S_{200\langle a_i b_i c_i\rangle}$ for the 200 sub-sets.

At $\Sigma_{11} = 300$ MPa, the 200⟨010⟩ and 200⟨021⟩ sub-sets have a decreasing *NARSS*. While in the 200⟨011⟩ sub-set, *NARSS* first increases and then decreases. At the end of loading this results in nearly equal values for $\langle\sum_s|\dot{\gamma}^s|\rangle$ for these three sub-sets. Consequently, these sub-sets have a similar lattice strain increment rate towards the end of loading. The combined effect of all these responses is a slightly larger spread in $S_{200\langle a_i b_i c_i\rangle}$ and a faster lattice strain increment rate in the 200 family. For $R = 0$ and $R = -0.37$, the difference in the evolution of $\langle\sum_s|\dot{\gamma}^s|\rangle$ and *NARSS* between different 200 sub-sets is much smaller than for $R = 1$. This explains the narrower spread in $S_{200\langle a_i b_i c_i\rangle}$ for these loadings. If we neglect the noisy behavior of the 200⟨031⟩ sub-set, then the trend in the lattice strain magnitudes in the plastic regime from the highest to lowest is 200⟨010⟩, 200⟨021⟩ and 200⟨011⟩ for $R = -0.37$ and $R = 1$. For $R = 0$, this is 200⟨010⟩, 200⟨011⟩ and 200⟨021⟩. The differences in lattice strain magnitudes for $R = 0$ and -0.37 are however very small and will be influenced by changes in local microstructure.

The lattice strain evolution in 220 sub-sets in the plastic regime shows different behavior for different R (see Fig. 8d, e and f). In the elastic regime, for $R = 0$ at the end of loading, this trend becomes 220⟨1$\bar{1}$1⟩, 220⟨3$\bar{3}$1⟩, 220⟨1$\bar{1}$3⟩, 220⟨001⟩ and 220⟨1$\bar{1}$0⟩. For $R = -0.37$, at the end of loading the trend from most compliant to stiffest sub-sets is 220⟨001⟩, 220⟨3$\bar{3}$1⟩, 220⟨1$\bar{1}$3⟩, 220⟨1$\bar{1}$0⟩ and 220⟨1$\bar{1}$1⟩. For $R = 1$, at the end of loading the trend from most compliant to stiffest sub-sets is 220⟨3$\bar{3}$1⟩, 220⟨1$\bar{1}$0⟩, 220⟨1$\bar{1}$1⟩, 220⟨001⟩ and 220⟨1$\bar{1}$3⟩. Furthermore, for $R = 0$ and $R = -0.37$, the average lattice strain of the 220 family in the plastic regime is lower than most of its sub-sets. This implies that there are other sub-sets having lower lattice strains values. Note that the coupled effect of elastic anisotropy and crystal orientation plays an important role in the lattice strain evolution of the 220 sub-sets in the plastic regime. A general trend in the lattice strain evolution of different sub-sets of 220 grains as a function of R is however not evident in the plastic regime. A similar analysis, as done in the case of 200 sub-sets for $R = 1$, can be performed for the 220 sub-sets and other grain families to understand their lattice strain evolution as a function of R. This is, however, beyond the scope of present work.

6. Conclusions

In this work, an FE-FFT multi-scale approach is proposed to quantitatively understand the lattice strain evolution of 316L stainless steel subjected to: (a) uniaxial tension in dog-bone samples $\frac{\Sigma_{22}}{\Sigma_{11}} = R = 0$, (b) uniaxial loading in cruciform samples with $R = -0.23$ in the elastic regime and $R = -0.37$ in the plastic regime, and (c) equibiaxial loading in cruciform samples $R = 1$. Experimental load and boundary conditions are supplied to the macroscopic FE model. The predicted macroscopic gauge stresses are imposed as homogeneous boundary conditions for the meso-scale EVPFFT model. The predicted lattice strains are compared with experimental values obtained from in-situ neutron diffraction measurements.

The main conclusions from this study are:

1) The FE-FFT approach successfully exploits and extends existing synergy between experiments and multi-scale modeling to capture the experimentally observed lattice strain evolution in the 111, 200, 220 and 311 grain families for all R.
2) A biaxial stress ratio dependent expression for the single crystal directional elastic compliance of the *hkl* grain families and their sub-sets is developed. The expression shows that for $R \neq 0$, the grain orientation in the {220} and {311} planes contributes to the directional elastic compliance (computed along the normal to these planes) of the sub-sets of 220 and 311 grain families, respectively. Furthermore, these contributions occur only for elastically anisotropic crystals and are weighed according to the value of R. In contrast, the directional elastic compliance of the sub-sets of 200 and 111 grain families is independent of the grain orientation in the {200} and {111} planes, respectively, and depends only on R.
3) In the elastic regime, the ordering of *hkl* grain families from the most compliant to the stiffest is 200, 311, 220 and 111 for all R. The spread in lattice strain evolution between different grain families decreases as R increases from −0.23 to 1. In contrast, the spread in lattice strain evolution between the sub-sets of each *hkl* grain family decreases with decreasing R. In the polycrystalline case, elastic interactions with grain neighborhoods and load sharing between and within the grain families result in a narrower spread in the lattice strain evolution. The lattice strain evolution trends are however similar for both single crystal and polycrystalline cases.
4) The resolved shear stress and the plastic slip activity within each sub-set of an *hkl* grain family depends on the orientation of the sub-set with respect to the biaxial loading directions and the magnitude of R. Together they determine the lattice strain evolution in the plastic regime, however, a trend in the lattice strain evolution is not evident.
5) For $R = 0$, −0.23 and −0.37, the lattice strain evolution in the 311 family is representative of the average polycrystalline response. For $R = 1$, the lattice strain evolution in all grain families is representative of the polycrystalline response.

Acknowledgements

MVU and HVS thank the European Research Council for financial support within the ERC-advanced grant MULTIAX (339245).

Appendix

A. Elastic strain response of a biaxially loaded cubic crystal.

In this appendix we derive the elastic strain response of a cubic crystal subjected to biaxial stress state along two orthonormal directions $[u_1v_1w_1]$ and $[u_2v_2w_2]$ defined in the reference frame XYZ of that crystal. We follow a procedure similar to that in the dissertation of Oliver [42].

The stresses and strains denoted in the Voigt notation such that:

$$\sigma_{ij} = \begin{pmatrix} \sigma_1 & \sigma_6 & \sigma_5 \\ \sigma_6 & \sigma_2 & \sigma_4 \\ \sigma_5 & \sigma_4 & \sigma_3 \end{pmatrix} \text{ and } \varepsilon_{ij} = \begin{pmatrix} \varepsilon_1 & \frac{1}{2}\varepsilon_6 & \frac{1}{2}\varepsilon_5 \\ \frac{1}{2}\varepsilon_6 & \varepsilon_2 & \frac{1}{2}\varepsilon_4 \\ \frac{1}{2}\varepsilon_5 & \frac{1}{2}\varepsilon_4 & \varepsilon_3 \end{pmatrix} \tag{A.1}$$

Let an orthonormal reference frame X′Y′Z′ be defined such that X′ is parallel to $[u_1v_1w_1]$ and Y′ is parallel to $[u_2v_2w_2]$. Clearly, Z′ is parallel to the common normal to $[u_1v_1w_1]$ and $[u_2v_2w_2]$. In this frame, let the stress tensor be defined as:

$$\boldsymbol{\sigma}' = \begin{pmatrix} \sigma_1 & 0 & 0 \\ 0 & \sigma_2 & 0 \\ 0 & 0 & 0 \end{pmatrix} \tag{A.2}$$

The VM stress for this single crystal is given as

$$\sigma_{VM} = \sqrt{\sigma_1^2 + \sigma_1\sigma_2 + \sigma_2^2} \tag{A.3}$$

In the XYZ reference frame, the stress tensor is given as,

$$\boldsymbol{\sigma} = \boldsymbol{a}^{\boldsymbol{T}}\boldsymbol{\sigma}'\boldsymbol{a} \tag{A.4}$$

where the transformation matrix is given as,

$$\boldsymbol{a} = \begin{pmatrix} u_1 & v_1 & w_1 \\ u_2 & v_2 & w_2 \\ (v_1w_2 - v_2w_1) & (u_2w_1 - u_1w_2) & (u_1v_2 - u_2v_1) \end{pmatrix} \tag{A.5}$$

Substituting (A.5) in (A.4) gives,

$$\boldsymbol{\sigma} = \begin{pmatrix} u_1^2\sigma_1 + u_2^2\sigma_2 & u_1v_1\sigma_1 + u_2v_2\sigma_2 & u_1w_1\sigma_1 + u_2w_2\sigma_2 \\ u_1v_1\sigma_1 + u_2v_2\sigma_2 & v_1^2\sigma_1 + v_2^2\sigma_2 & v_1w_1\sigma_1 + v_2w_2\sigma_2 \\ u_1w_1\sigma_1 + u_2w_2\sigma_2 & v_1w_1\sigma_1 + v_2w_2\sigma_2 & w_1^2\sigma_1 + w_2^2\sigma_2 \end{pmatrix} \tag{A.6}$$

Let s_{ij} represent the elastic compliance matrix in the Voigt notation. Then the strain matrix elements are given by the Hooke's law in Voigt notation as,

$$\begin{aligned} \varepsilon_i = s_{ij}\sigma_j &= \begin{pmatrix} s_{11} & s_{12} & s_{12} & 0 & 0 & 0 \\ s_{12} & s_{11} & s_{12} & 0 & 0 & 0 \\ s_{12} & s_{12} & s_{11} & 0 & 0 & 0 \\ 0 & 0 & 0 & s_{44} & 0 & 0 \\ 0 & 0 & 0 & 0 & s_{44} & 0 \\ 0 & 0 & 0 & 0 & 0 & s_{44} \end{pmatrix} \begin{pmatrix} u_1^2\sigma_1 + u_2^2\sigma_2 \\ v_1^2\sigma_1 + v_2^2\sigma_2 \\ w_1^2\sigma_1 + w_2^2\sigma_2 \\ v_1w_1\sigma_1 + v_2w_2\sigma_2 \\ u_1w_1\sigma_1 + u_2w_2\sigma_2 \\ u_1v_1\sigma_1 + u_2v_2\sigma_2 \end{pmatrix} \\ &= \begin{pmatrix} s_{11}\left(u_1^2\sigma_1 + u_2^2\sigma_2\right) + s_{12}\left[\left(v_1^2 + w_1^2\right)\sigma_1 + \left(v_2^2 + w_2^2\right)\sigma_2\right] \\ s_{11}\left(v_1^2\sigma_1 + v_2^2\sigma_2\right) + s_{12}\left[\left(u_1^2 + w_1^2\right)\sigma_1 + \left(u_2^2 + w_2^2\right)\sigma_2\right] \\ s_{11}\left(w_1^2\sigma_1 + w_2^2\sigma_2\right) + s_{12}\left[\left(u_1^2 + v_1^2\right)\sigma_1 + \left(u_2^2 + v_2^2\right)\sigma_2\right] \\ s_{44}(v_1w_1\sigma_1 + v_2w_2\sigma_2) \\ s_{44}(u_1w_1\sigma_1 + u_2w_2\sigma_2) \\ s_{44}(u_1v_1\sigma_1 + u_2v_2\sigma_2) \end{pmatrix} \end{aligned} \tag{A.7}$$

The strain resolved along the $\vec{g} = [hkl]$ direction is given as,

$$\varepsilon_{hkl} = \frac{1}{|\vec{g}|^2}\varepsilon_{ij}g_i g_j = \frac{1}{|\vec{g}|^2}\left[h^2\varepsilon_{11} + k^2\varepsilon_{22} + l^2\varepsilon_{33} + 2kl\varepsilon_{23} + 2hl\varepsilon_{13} + 2hk\varepsilon_{12}\right] = \frac{1}{|\vec{g}|^2}\left[h^2\varepsilon_1 + k^2\varepsilon_2 + l^2\varepsilon_3 + kl\varepsilon_4 + hl\varepsilon_5 + hk\varepsilon_6\right] \tag{A.8}$$

After some algebra it can be shown that the strain tensor resolved along the *hkl* direction is given as,

$$\varepsilon_{hkl} = s_{11}[A_1\sigma_1 + A_2\sigma_2] + s_{12}[(1-A_1)\sigma_1 + (1-A_2)\sigma_2] + s_{44}[B_1\sigma_1 + B_2\sigma_2] \tag{A.9}$$

where,

$$A_1 = \frac{1}{|\vec{g}|^2}\left[h^2u_1^2 + k^2v_1^2 + l^2w_1^2\right] \tag{A.10}$$

$$A_2 = \frac{1}{|\vec{g}|^2}\left[h^2u_2^2 + k^2v_2^2 + l^2w_2^2\right] \tag{A.11}$$

$$B_1 = \frac{1}{|\vec{g}|^2}[hku_1v_1 + hlu_1w_1 + klv_1w_1] \tag{A.12}$$

$$B_2 = \frac{1}{|\vec{g}|^2}[hku_2v_2 + hlu_2w_2 + klv_2w_2] \tag{A.13}$$

Finally note that,

$$A_1 + 2B_1 = \frac{1}{|\vec{g}|^2}\left[h^2u_1^2 + k^2v_1^2 + l^2w_1^2 + 2(hku_1v_1 + hlu_1w_1 + klv_1w_1)\right] = \frac{1}{|\vec{g}|^2}(hu_1 + kv_1 + lw_1)^2 \tag{A.14}$$

$$A_2 + 2B_2 = \frac{1}{|\vec{g}|^2}\left[h^2u_2^2 + k^2v_2^2 + l^2w_2^2 + 2(hku_2v_2 + hlu_2w_2 + klv_2w_2)\right] = \frac{1}{|\vec{g}|^2}(hu_2 + kv_2 + lw_2)^2 \tag{A.15}$$

Let *hkl* be parallel to $[u_1v_1w_1]$ such that $u_1 = \frac{h}{\sqrt{h^2+k^2+l^2}}$, $v_1 = \frac{k}{\sqrt{h^2+k^2+l^2}}$ and $w_1 = \frac{l}{\sqrt{h^2+k^2+l^2}}$, and hence perpendicular to $[u_2v_2w_2]$. This implies that $A_1 + 2B_1 = 1$ and $A_2 + 2B_2 = 0$. Substituting for $A_1 = 1 - 2B_1$ and $2B_2 = 1 - A_2$ in Eq. (A.9) gives,

$$\varepsilon_{hkl} = \varepsilon_{u_1v_1w_1} = \left[s_{11} - 2\left(s_{11} - s_{12} - \frac{s_{44}}{2}\right)\left(u_1^2v_1^2 + u_1^2w_1^2 + v_1^2w_1^2\right)\right]\sigma_1 + \left[s_{12} + \left(s_{11} - s_{12} - \frac{s_{44}}{2}\right)\left(u_1^2u_2^2 + v_1^2v_2^2 + w_1^2w_2^2\right)\right]\sigma_2 \tag{A.16}$$

I. Uniaxial loading

When $\sigma_2 = 0$, Eq. (A.16) can be reduced to the well-known expression on elastic stiffness parallel to the loading direction [42]:

$$\frac{\varepsilon_{hkl}}{\sigma_1} = s_{11} - 2\left(s_{11} - s_{12} - \frac{s_{44}}{2}\right)\left(u_1^2v_1^2 + u_1^2w_1^2 + v_1^2w_1^2\right) \tag{A.17}$$

1. $[u_1v_1w_1] \parallel [200]$

Substituting in Eq. (A.17) gives,

$$\frac{\varepsilon_{200}}{\sigma_1} = s_{11} \tag{A.18}$$

The elastic strain along this direction is independent of the elastic anisotropy of the material.

2. $[u_1v_1w_1] \parallel [220]$

Substituting in Eq. (A.17) gives,

$$\frac{\varepsilon_{220}}{\sigma_1} = s_{11} - \frac{1}{2}\left(s_{11} - s_{12} - \frac{S_{44}}{2}\right) \tag{A.19}$$

When $\sigma_1 = 0$, Eq. (A.16) can be reduced to the well-known expression on elastic stiffness perpendicular to the loading direction [42]:

$$\frac{\varepsilon_{hkl}}{\sigma_2} = s_{12} + \left(s_{11} - s_{12} - \frac{s_{44}}{2}\right)\left(u_1^2u_2^2 + v_1^2v_2^2 + w_1^2w_2^2\right) \tag{A.20}$$

II. General biaxial loading

Rewriting Eq. (A.16) as,

$$\frac{\varepsilon_{hkl}}{\sigma_1} = s_{11} + \frac{\sigma_2}{\sigma_1}s_{12} + \left(s_{11} - s_{12} - \frac{s_{44}}{2}\right)\left[\frac{\sigma_2}{\sigma_1}\left(u_1^2u_2^2 + v_1^2v_2^2 + w_1^2w_2^2\right) - 2\left(u_1^2v_1^2 + u_1^2w_1^2 + v_1^2w_1^2\right)\right] \tag{A.21}$$

Eq. (A.21) is the directional elastic compliance along the measurement direction during biaxial loading.

1. $[u_1v_1w_1] \parallel [200]$

Eq. (A.21) reduces to

$$\frac{\varepsilon_{200}}{\sigma_1} = s_{11} + \frac{\sigma_2}{\sigma_1}s_{12} \tag{A.22}$$

2. $[u_1v_1w_1] \parallel [220]$

Eq. (A.21) becomes

$$\frac{\varepsilon_{220}}{\sigma_1} = s_{11} + \frac{\sigma_2}{\sigma_1}s_{12} + \frac{1}{2}\left(s_{11} - s_{12} - \frac{s_{44}}{2}\right)\left[\left(1 - w_2^2\right)\frac{\sigma_2}{\sigma_1} - 1\right] \tag{A.23}$$

3. $[u_1 v_1 w_1] \parallel [111]$

Eq. (A.21) gives.

$$\frac{\varepsilon_{111}}{\sigma_1} = s_{11} + \frac{\sigma_2}{\sigma_1}s_{12} + \left(s_{11} - s_{12} - \frac{s_{44}}{2}\right)\frac{1}{3}\left[\frac{\sigma_2}{\sigma_1} - 2\right] \tag{A.24}$$

4. $[u_1 v_1 w_1] \parallel [311]$

Eq. (A.21) gives

$$\frac{\varepsilon_{311}}{\sigma_1} = s_{11} + \frac{\sigma_2}{\sigma_1}s_{12} + \left(s_{11} - s_{12} - \frac{s_{44}}{2}\right)\left[\frac{\sigma_2}{\sigma_1}\left(\frac{8}{11}u_2^2 + \frac{1}{11}\right) - \frac{38}{121}\right] \tag{A.25}$$

The elastic strain along different directions is dependent on both elastic anisotropy and the load ratio σ_2/σ_1.

References

[1] C.C. Tasan, J.P.M. Hoefnagels, E.C.A. Dekkers, M.G.D. Geers, Multi-Axial deformation setup for microscopic testing of sheet metal to fracture, Exp. Mech. 52 (2012) 669–678, http://dx.doi.org/10.1007/s11340-011-9532-x.

[2] T. Kuwabara, S. Ikeda, K. Kuroda, Measurement and analysis of differential work hardening in cold-rolled steel sheet under biaxial tension, J. Mater. Process. Technol. 80–81 (1998) 517–523, http://dx.doi.org/10.1016/S0924-0136(98)00155-1.

[3] T. Kuwabara, M. Kuroda, V. Tvergaard, K. Nomura, Use of abrupt strain path change for determining subsequent yield surface: experimental study with metal sheets, Acta Mater. 48 (2000) 2071–2079, http://dx.doi.org/10.1016/S1359-6454(00)00048-3.

[4] T. Kuwabara, K. Yoshida, K. Narihara, S. Takahashi, Anisotropic plastic deformation of extruded aluminum alloy tube under axial forces and internal pressure, Int. J. Plast. 21 (2005) 101–117, http://dx.doi.org/10.1016/j.ijplas.2004.04.006.

[5] T. Kuwabara, Advances in experiments on metal sheets and tubes in support of constitutive modeling and forming simulations, Int. J. Plast. 23 (2007) 385–419, http://dx.doi.org/10.1016/j.ijplas.2006.06.003.

[6] A. Hannon, P. Tiernan, A review of planar biaxial tensile test systems for sheet metal, J. Mater. Process. Technol. 198 (2008) 1–13, http://dx.doi.org/10.1016/j.jmatprotec.2007.10.015.

[7] F. Abu-Farha, L.G. Hector, M. Khraisheh, Cruciform-shaped specimens for elevated temperature biaxial testing of lightweight materials, J. Min. Met. Mater. Soc. 61 (2009) 48–56.

[8] A. Makinde, L. Thibodeau, K.W. Neale, D. Lefebvre, Design of a biaxial extensometer for measuring strains in cruciform specimens, Exp. Mech. 32 (1992) 132–137, http://dx.doi.org/10.1007/BF02324724.

[9] A. Makinde, L. Thibodeau, K.W. Neale, Development of an apparatus for biaxial testing using cruciform specimens, Exp. Mech. 32 (1992) 138–144, http://dx.doi.org/10.1007/BF02324725.

[10] S.R. MacEwen, R. Perrin, D. Green, A. Makinde, K.W. Neale, An evaluation of planar biaxial deformation in H19 can-stock sheet, in: Proc. 13th Risø Int. Symp. Mater. Sci., Risø National Laboratory, Roskilde, Denmark, 1992, pp. 539–545.

[11] E. Hoferlin, A. Van Bael, P. Van Houtte, G. Steyaert, C. De Maré, Biaxial tests on cruciform specimens for the validation of crystallographic yield loci, J. Mater. Process. Technol. 80–81 (1998) 545–550, http://dx.doi.org/10.1016/S0924-0136(98)00123-X.

[12] V. Bonnand, J.L. Chaboche, P. Gomez, P. Kanouté, D. Pacou, Investigation of multiaxial fatigue in the context of turboengine disc applications, Int. J. Fatigue 33 (2011) 1006–1016, http://dx.doi.org/10.1016/j.ijfatigue.2010.12.018.

[13] R.A. Cláudio, L. Reis, M. Freitas, Biaxial high-cycle fatigue life assessment of ductile aluminium cruciform specimens, Theor. Appl. Fract. Mech. 73 (2014) 82–90, http://dx.doi.org/10.1016/j.tafmec.2014.08.007.

[14] D.E. Green, K.W. Neale, S.R. MacEwen, A. Makinde, R. Perrin, Experimental investigation of the biaxial behaviour of an aluminum sheet, Int. J. Plast. 20 (2004) 1677–1706, http://dx.doi.org/10.1016/j.ijplas.2003.11.012.

[15] Y. Hanabusa, H. Takizawa, T. Kuwabara, Numerical verification of a biaxial tensile test method using a cruciform specimen, J. Mater. Process. Technol. 213 (2013) 961–970, http://dx.doi.org/10.1016/j.jmatprotec.2012.12.007.

[16] N. Deng, T. Kuwabara, Y.P. Korkolis, Cruciform specimen design and verification for constitutive identification of anisotropic sheets, Exp. Mech. 55 (2015) 1005–1022, http://dx.doi.org/10.1007/s11340-015-9999-y.

[17] T. Foecke, M.A. Iadicola, A. Lin, S.W. Banovic, A Method for direct measurement of multiaxial stress-strain curves in sheet metal, Metall. Mater. Trans. A 38 (2007) 306–313, http://dx.doi.org/10.1007/s11661-006-9044-y.

[18] M.A. Iadicola, T. Foecke, S.W. Banovic, Experimental observations of evolving yield loci in biaxially strained AA5754-O, Int. J. Plast. 24 (2008) 2084–2101, http://dx.doi.org/10.1016/j.ijplas.2008.03.003.

[19] M.A. Iadicola, A.A. Creuziger, T. Foecke, Advanced biaxial cruciform testing at the NIST center for automotive lightweighting, in: M. Rossi, M. Sasso, N. Connesson, R. Singh, A. DeWald, D. Backman, P. Gloeckner (Eds.), Residual Stress Thermomechanics Infrared Imaging Hybrid Tech. Inverse Probl., Proc. 2013 Annu. Conf. Exp. Appl. Mech., Vol. 8, Springer International Publishing, Cham, 2014, pp. 277–285, http://dx.doi.org/10.1007/978-3-319-00876-9_34.

[20] T. Lorentzen, M.T. Hutchings, P.J. Withers, T.M. Holden, Introduction to the Characterization of Residual Stress by Neutron Diffraction, CRC Press, 2005.

[21] D.M. Collins, M. Mostafavi, R.I. Todd, T. Connolley, A.J. Wilkinson, A synchrotron X-ray diffraction study of in situ biaxial deformation, Acta Mater. 90 (2015) 46–58, http://dx.doi.org/10.1016/j.actamat.2015.02.009.

[22] S. Van Petegem, J. Wagner, T. Panzner, M.V. Upadhyay, T.T.T. Trang, H. Van Swygenhoven, In-situ neutron diffraction during biaxial deformation, Acta Mater. 105 (2016) 404–416, http://dx.doi.org/10.1016/j.actamat.2015.12.015.

[23] J. Repper, M. Niffenegger, S. Van Petegem, W. Wagner, H. Van Swygenhoven, In-situ biaxial mechanical testing at the neutron time-of-flight diffractometer POLDI, Mater. Sci. Forum. 768–769 (2013) 60–65 doi:http://dx.doi.org/10.4028, www.scientific.net/MSF.768-769.60.

[24] J.A. Wollmershauser, B. Clausen, S.R. Agnew, A slip system-based kinematic hardening model application to in situ neutron diffraction of cyclic deformation of austenitic stainless steel, Int. J. Fatigue 36 (2012) 181–193, http://dx.doi.org/10.1016/j.ijfatigue.2011.07.008.

[25] C.J. Neil, J.A. Wollmershauser, B. Clausen, C.N. Tomé, S.R. Agnew, Modeling lattice strain evolution at finite strains and experimental verification for copper and stainless steel using in situ neutron diffraction, Int. J. Plast. 26 (2010) 1772–1791, http://dx.doi.org/10.1016/j.ijplas.2010.03.005.

[26] A.A. Saleh, E.V. Pereloma, B. Clausen, D.W. Brown, C.N. Tomé, A.A. Gazder, Self-consistent modelling of lattice strains during the in-situ tensile loading of twinning induced plasticity steel, Mater. Sci. Eng. A 589 (2014) 66–75, http://dx.doi.org/10.1016/j.msea.2013.09.073.

[27] H. Wang, B. Clausen, C.N. Tomé, P.D. Wu, Studying the effect of stress relaxation and creep on lattice strain evolution of stainless steel under tension, Acta Mater. 61 (2013) 1179–1188, http://dx.doi.org/10.1016/j.actamat.2012.10.027.

[28] R.A. Lebensohn, A.K. Kanjarla, P. Eisenlohr, An elasto-viscoplastic formulation based on Fast Fourier transforms for the prediction of micromechanical fields in polycrystalline materials, Int. J. Plast. 32–33 (2012) 59–69.

[29] A.K. Kanjarla, R.A. Lebensohn, L. Balogh, C.N. Tomé, Study of internal lattice strain distributions in stainless steel using a full-field elasto-viscoplastic formulation based on fast Fourier transforms, Acta Mater. 60 (2012) 3094–3106, http://dx.doi.org/10.1016/j.actamat.2012.02.014.

[30] D.-F. Li, N.P. O'Dowd, On the evolution of lattice deformation in austenitic stainless steels—The role of work hardening at finite strains, J. Mech. Phys. Solids 59 (2011) 2421–2441, http://dx.doi.org/10.1016/j.jmps.2011.09.008.

[31] ABAQUS Documentation, Dassault Systèmes, Providence, RI, USA, 2011.

[32] J. Kochmann, S. Wulfinghoff, S. Reese, J.R. Mianroodi, B. Svendsen, Two-scale FE–FFT- and phase-field-based computational modeling of bulk microstructural evolution and macroscopic material behavior, Comput. Methods Appl. Mech. Eng. 305 (2016) 89–110, http://dx.doi.org/10.1016/j.cma.2016.03.001.

[33] U. Stuhr, Time-of-flight diffraction with multiple pulse overlap. Part I: the concept, Nucl. Instrum. Methods Phys. Res. Sect. Accel. Spectrom. Detect. Assoc. Equip. 545 (2005) 319–329, http://dx.doi.org/10.1016/j.nima.2005.01.320.

[34] U. Stuhr, H. Spitzer, J. Egger, A. Hofer, P. Rasmussen, D. Graf, A. Bollhalder, M. Schild, G. Bauer, W. Wagner, Time-of-flight diffraction with multiple frame overlap Part II: the strain scanner POLDI at PSI, Nucl. Instrum. Methods Phys. Res. Sect. Accel. Spectrom. Detect. Assoc. Equip. 545 (2005) 330–338, http://dx.doi.org/10.1016/j.nima.2005.01.321.

[35] O. Arnold, J.C. Bilheux, J.M. Borreguero, A. Buts, S.I. Campbell, L. Chapon, M. Doucet, N. Draper, R. Ferraz Leal, M.A. Gigg, V.E. Lynch, A. Markvardsen, D.J. Mikkelson, R.L. Mikkelson, R. Miller, K. Palmen, P. Parker, G. Passos, T.G. Perring, P.F. Peterson, S. Ren, M.A. Reuter, A.T. Savici, J.W. Taylor, R.J. Taylor, R. Tolchenov, W. Zhou, J. Zikovsky, Mantid—Data analysis and visualization package for neutron scattering and SR experiments, Nucl. Instrum. Methods Phys. Res. Sect. Accel. Spectrom. Detect. Assoc. Equip. 764 (2014) 156–166, http://dx.doi.org/10.1016/j.nima.2014.07.029.

[36] R.A. Lebensohn, N-site modeling of a 3D viscoplastic polycrystal using Fast Fourier Transform, Acta Mater. 49 (2001) 2723–2737.

[37] C. Tome, G.R. Canova, U.F. Kocks, N. Christodoulou, J.J. Jonas, The relation

between macroscopic and microscopic strain hardening in F.C.C. polycrystals, Acta Metall. 32 (1984) 1637–1653, http://dx.doi.org/10.1016/0001-6160(84)90222-0.

[38] D. Gonzalez, J.F. Kelleher, J. Quinta da Fonseca, P.J. Withers, Macro and intergranular stress responses of austenitic stainless steel to 90° strain path changes, Mater. Sci. Eng. A 546 (2012) 263–271, http://dx.doi.org/10.1016/j.msea.2012.03.064.

[39] A.K. Kanjarla, R.A. Lebensohn, L. Balogh, C.N. Tomé, Study of internal lattice strain distributions in stainless steel using a full-field elasto-viscoplastic formulation based on Fast Fourier Transforms, Acta Mater. 60 (2012) 3094–3106.

[40] B. Clausen, Characterization of Polycrystal Deformation by Numerical Modelling and Neutron Diffraction Measurements, Technical University of Denmark and Risoe National Laboratory, 1997.

[41] Iso Standard ISO/TS 21432, (E): Non-destructive Testing - Standard Test Method for Determining Residual Stresses by Neutron Diffraction, 2005.

[42] E.C. Oliver, The Generation of Internal Stresses in Single and Two Phase Materials, University of Manchester, 2002.

[43] E.C. Oliver, M.R. Daymond, P.J. Withers, Interphase and intergranular stress generation in carbon steels, Acta Mater. 52 (2004) 1937–1951.